Thesis for the degree
Doctor of Philosophy

Submitted to the Scientific Council of the
Weizmann Institute of Science
Rehovot, Israel

עבודת גמר (תזה) לתואר
דוקטור לפילוסופיה

מוגשת למועצה המדעית של
מכון ויצמן למדע
רחובות, ישראל

במתכונת "מאמרים"
In a "Published Papers" Format

By
Haim Beidenkopf

מאת
חיים ביידנקופף

תרמודינמיקה ודינמיקה של מעבר הפאזה הזכוכיתי מסדר שני של מערבולות הזרם ב- $Bi_2Sr_2CaCu_2O_8$

Thermodynamics and Dynamics of the Second-order Vortex Glass Transition in $Bi_2Sr_2CaCu_2O_8$

Advisor:
Prof. Eli Zeldov

מנחה:
פרופ' אלי זלדוב

July, 2009

תמוז, תשס"ט

Summary

The vortex matter in the high transition temperature superconductor $Bi_2Sr_2CaCu_2O_8$ offers a system in which interactions, thermal fluctuations, and quenched disorder closely compete, giving rise to an intricate thermodynamic phase diagram. Early on the notion of a perfectly ordered Abrikosov vortex lattice was abandoned in favor of the quasi-ordered Bragg glass. Thermal fluctuations at high temperatures and random pinning at low temperatures and high vortex-densities destabilize further the Bragg glass phase, giving rise to an amorphous vortex configuration. We found evidence of a novel second-order glass transition in the local magnetization, made reversible by the application of vortex shaking. It further splits the phase diagram into four distinct phases: At high fields reside the amorphous liquid and glass vortex phases. At low fields the glass line separates a Bragg glass from a thermally depinned variant of it, possibly reintroducing long-range spatial correlations of a vortex lattice phase.

The novel glass transition, and particularly the intriguing thermally depinned Bragg glass phase, called for further characterization. We thus studied the evolution of the glass line with oxygen doping, which enhances the coupling between the superconducting layers of $Bi_2Sr_2CaCu_2O_8$, while introducing additional pinning centers to it. Surprisingly, we found that the glass line evolves according to a simple disorder-free scaling law together with the thermally induced part of the melting line. Further insight came from a theoretical model that was found to describe well the experimental phase diagram. We found that the reduced anisotropy with doping reduces the role of pinning, even though it becomes more abundant. To complement this, we initiated a study of the phase-diagram dependence on the defect density, which we found to be greatly enhanced via proton irradiation.

The vortex dynamics within the thermally-depinned phases and close to the glassy phase boundary was studied next. The nonlinear parasitic contribution arising from the dynamical response along the c-axis was eliminated via a novel ion-irradiation scheme. As transport sensitivity does not suffice for studying the exponentially-small resistivity at such low temperature, we devised an indirect approach for extracting the bulk resis-

tance. In it, we monitor the current distribution in the sample, which results from the interplay between the thermally-activated resistances and geometrical inductances of the sample bulk and edges. We first resolved the electrodynamic nature of the T_x transition, below which the edge inductance dominates the sample impedance. Then, we used the depinning transition, T_d, below which only the ratio between bulk and edge inductances determines the flow pattern, to reproduce the bulk resistance. Unlike vortex liquid, the lattice phase results in a non-Ohmic resistance. However, preliminary results do not seem to indicate the glassy resistance predicted for the Bragg glass. In addition, the temperature dependence of the resistance showed deviation from a thermally activated behavior as the glass line was approached both from within the liquid and the lattice phases, signaling criticality.

Contents

Acknowledgements

I thank my advisor, Eli Zeldov, for sharing with me his vast knowledge and wisdom, for his patience and kindness, and for his constant support all along the way.

I thank Yuri Myasoedov for his great advice which, together with his his skillful hands, helped remove obstacles and accomplish the research goals.

I thank my past and present lab colleagues Nurit, Tal, Sarah, Amit, Yehonathan, Beena, Dima, Ilia and Satya for numerous fruitful discussions and for making this period so enjoyable.

Special thanks go to my beloved wife and daughter, and to my close family and friends for supporting me throughout this journey.

1. Introduction

The various energy scales and processes that contribute to the diverse thermodynamics and dynamics of the vortex matter in $Bi_2Sr_2CaCu_2O_8$ are portrayed below. Superconductivity and the resulting vorticity are introduced first. Then we describe the inter-vortex interactions, and various sources of fluctuations in the system. Finally, the vortex response to an external force and finite size effects are discussed.

1.1 Superconductivity

Superconductivity is an intriguing electronic state in which below a critical transition temperature, T_c, the electrons condense into the seemingly bosonic ground state as a superfluid despite their fermionic statistics. As shown in the BCS theory of superconductivity [1], the Fermi surface develops an instability in the presence of an attractive electronic interaction, which in conventional superconductors is mediated by phonons. As a result, time-reversal-symmetric pairs of electrons in the vicinity of the Fermi surface form, so-called, Cooper pairs and condense. The fermionic nature of the electrons, however, is still retained as the separation between paired electrons, termed the coherence length and denoted by ξ, is larger than the inter-electronic separation by 2-3 orders of magnitude. Accordingly, the Fermi sphere does not collapse, but an excitation energy gap opens below T_c about its surface. This gap permits the dissipationless flow of a supercurrent [2].

In high-T_c superconductors in general, and specifically in $Bi_2Sr_2CaCu_2O_8$, the exact pairing mechanism seems to be different, though it is yet unknown. It results in a more complex phenomenological picture, that includes a pseudo-gap that survives above the superconducting transition temperature [3] and may even indicate the existence of competing ground states [4, 5]. Nevertheless, the pairing of electrons itself is essential for obtaining a superfluid behavior in a fermionic system. Another characteristics of the cuprate family to which $Bi_2Sr_2CaCu_2O_8$ belongs is their layered structure, in which the two-dimensional CuO_2 planes are the ones that superconduct. This results in a

pronounced anisotropy between the in- and out-of-plane directions, which may be modified by the oxygen doping level [6]. $Bi_2Sr_2CaCu_2O_8$ is the most extreme among the cuprates in that sense because its CuO_2 double-layers separation is comparable to the coherence length. Therefore, it is usually treated as a truly layered compound, rather than anisotropic.

1.2 Vorticity

Breaking time reversal symmetry by the introduction of an external magnetic field breaks the electronic pairing. At low magnetic fields the system maintains its superconducting state by driving supercurrents that exactly cancel the applied field within the sample, which is known as the Meissner effect [7]. The sample manages to do so to within a certain screening distance, called the penetration depth and denoted by λ, from its surface. With increasing magnetic field the superconducting system invests more energy in its screening until a point is reached beyond which magnetic field screening is no longer beneficial energetically. At higher fields two scenarios may take place. In type I superconductors the system turns back normal. In type II superconductors, such as $Bi_2Sr_2CaCu_2O_8$, the energetic cost involved in flux expulsion is reduced by forming interfaces between superconducting and normal regions. To maximize such interfaces the system allows the penetration of magnetic flux in the form of vortices with normal cores of minimal volume (of radius ξ). The amount of magnetic flux carried by each vortex, $\Phi_\circ = hc/2e$, is quantized by the coherent condensate that surrounds it with a magnetic profile that decays radially due to circulating supercurrents along the typical screening radius λ. At high enough magnetic fields, at which the normal vortex cores begin to overlap, type II superconductors also turn normal. The layered structure of $Bi_2Sr_2CaCu_2O_8$ gives rise to two kinds of vortices depending on the orientation of the magnetic field: in the out-of-plane direction, two-dimensional pancake vortices form on the superconducting planes, stacked by weak inter-plane coupling [8]. In the in-plane direction, Josephson vortices are formed in the intrinsic Josephson junctions between the superconducting planes [9, 10]. At intermediate angles various vortex structures may form [11] such as kinked vortices [12] and the crossing lattices configuration [13].

1.3 Interactions

The shielding currents carried by two parallel vortices exert a repulsive inter-vortex Magnus force. It takes the form of a Lorentz repulsion between the shielding current of one

vortex and the magnetic flux carried by the other. Therefore, the mean-field ground state for a vortex system is in the Abrikosov lattice configuration [14] that minimizes the inter-vortex repulsion. Calculation shows that the triangular lattice is the most favorable, with a lattice constant of $a_\circ \approx \sqrt{\Phi_\circ/B}$. In practice, however, disordering pinning potential and elevated temperatures give rise to strong vortex fluctuations that compete with the vortex-matter elasticity.

1.4 Quenched disorder

Various defects in the crystalline ionic structure locally supress the superconducting order parameter. It therefore becomes energetically favorable to localize the vortex normal core on such defects, giving rise to an underlying random pinning potential for vortices. The resulting disordering energy landscape competes with the interactions that promote a vortex lattice configuration. It was predicted that the smallest amount of point pinning inevitably reduces the long-range vortex correlations of the lattice to quasi-long-ranged ones, characteristic of the Bragg glass phase [15, 16, 17]. This phase is quasi-ordered on one hand, but shows glassy dynamics with energy barriers that diverge with vanishing current on the other.

With increasing vortex density, which increases the role of disorder, the vortex matter was shown to undergo a disorder-induced first-order transition [18, 19, 20, 21] across which topological excitations in the form of vortex loops proliferate [22, 23]. This renders the vortex matter completely amorphous and glassy. However, direct study of the disorder-dominated regions of the vortex phase diagram is hindered by the diverging energy barriers between metastable states, that result in slow relaxation and off-equilibrium hysteretic behavior [24]. In addition to the dynamic-like vortex friction, pinning gives rise to a static friction in the form of a minimal critical current required to initiate vortex flow. According to the Bean model [25], the relaxation of a non-equilibrium current distribution associated with an off-equilibrium magnetization profile halts once the current drops below the critical current, which is the main source of hysteresis. While Bragg-glass and amorphous glassy phases are the only constituents of the phase diagram of low-T_c type II superconductors (such as $NbSe_2$ [26]), in high-T_c superconductors thermal fluctuations also play a dominant role introducing additional thermodynamic phases, as will be discussed below.

Disorder can be also introduced artificially by particle irradiation. While light elements such as electrons [27, 20] and protons [28, 29] increase the density of point-like defects, heavy ion irradiation leaves columnar defects along the particle tracks [30]. When

aligned in the out-of-plane direction these increase the c-axis correlations of vortices, once pinned, and thereby reduce the anisotropy of the layered materials [31]. In the presence of columnar defects the associated phase diagram is altered, consisting of an amorphous Bose glass phase at low temperature [32], while at high temperatures thermal fluctuations play the dominant role.

1.5 Thermal fluctuations

The discovery of high transition temperature superconductors [33] revolutionized the perception of superconductivity in terms of both applications and fundamental research, and with it the field of vortices. It allowed the study of vortex matter at elevated temperatures, at which vortices are subject to strong thermal fluctuations. On one hand, thermally assisted vortex excursions destabilize the vortex correlations within the ordered phase. On the other, they facilitate vortex depinning, thus rendering the disordering potential shallower. The material structure of layered two-dimensional planes enhances even further the role of thermal fluctuation.

This has a striking effect on the first-order disorder-induced transition. At first, with increasing temperature, the transition line shifts to higher vortex densities in order to meet the critical disordering strength in the presence of the shallower pinning potential [22, 34, 35, 36]. But then the line reaches a maximum and reverses its slope, signifying a smooth crossover from disorder to thermally induced first-order transition. Accordingly, at high temperature the (quasi) ordered phase melts into a vortex liquid phase [19, 37, 38, 39, 40]. The melting transition into the amorphous liquid state seems to occur simultaneously with a decoupling transition into a pancake vortex gas [41, 42, 43, 44].

At high enough temperatures, as the pinning potential weakens, the system manages to relax to its equilibrium state, and the hysteretic behavior is suppressed. Whether this crossover in the vortex relaxation signifies a thermodynamic depinning transition is a key issue targeted in the research reported herewith. At high magnetic field the possibility of a glass transition separating the glass from the liquid was previously accounted [37, 45, 46, 47, 48]. In contrast, the occurrence of such a depinning transition below the melting line was rarely considered [46, 47, 49, 50]. Theoretically, the Bragg glass phase was usually found to be stable under thermal fluctuations so long as topological excitations are excluded and the system is not treated as two-dimensional [51]. Thermal fluctuations have their effect also in ion-irradiated samples. Indeed, the Bose glass transition, above which vortices are thermally depinned from columnar defects and melt into liquid, was predicted [32] and later detected [52, 53].

1.6 External force

An externally-injected current applies a transverse Magnus (Lorentz) force on the individual vortices. As the vortices flow, they dissipate energy via electronic excitation within their normal cores. At high current densities this may become a dominant energetic consideration, extending the thermodynamic phase diagram to a dynamic one [54, 55, 56, 57, 58]. The scope of the research reported, however, is restricted to low current densities, which do not alter the thermodynamic phase diagram, but rather probe its dynamics.

The inter-vortex correlations, and even more so the pinning efficiency of the various thermodynamic vortex phases, give rise to diverse vortex dynamics. While the thermally-depinned vortex liquid has an Arrhenius Ohmic response [59], the resistivity of the glassy phase should vanish with vanishing current as the energy barriers separating metastable states diverge [48, 60, 61].

The material's anisotropy, imposed by its layered structure, complicates further the interpretation of the experimental results. As a result of this anisotropy, the current is distributed unevenly along the superconducting planes and perpendicular to them, where it has to tunnel across insulating buffers separating the superconducting planes [62]. This gives rise to high current densities that flow only a few layers near the surface through which current is injected, and therefore to strong current gradients across these few layers, that result in shear effects of pancake vortex stacks in the respective layers [63, 64].

1.7 Finite size

The macroscopic coherence of the superconducting state causes the finite size of an actual superconducting single crystal to be relevant even inside its bulk, and not just locally at its edges. Both the Meissner shielding currents have to adopt to the actual geometry of the sample, as well as the vortices that thread it. The interplay between the interaction between shielding currents and vortices and the vortex line tension results either in focusing or expulsion of vortices from the sample center according to the specific sample geometry. Consequently, the equilibrium magnetic induction, that sets the vortex density distribution, has a curved profile [65]. This geometric effect alone may result in hysteretic behavior. In the common platelet sample geometry, for instance, the Meissner currents focus vortices towards the center of the sample upon their entry. But then, on exiting the sample, vortices face a geometrical barrier, as they need to overcome that same focusing force.

Close to the sample edges, the vortices encounter another energetic surface barrier that impedes their motion [66]. It is imposed by the boundary conditions, satisfied by an image antivortex, which thus attract vortices towards the edge. The surface barrier is also asymmetric to vortex entry and exit, and thus serves as another source of hysteresis [67].

2. Methods

A study of the vortex matter phase diagram requires a broad experimental toolkit. Various mechanisms obscure the desired physical quantities such as the equilibrium magnetization or the bulk vortex dynamics of the different vortex phases. Therefore, novel techniques, which are the outcome of deep understanding of the processes involved and accurate modeling, are required in order to eliminate parasitic effects. Several such methods, which were developed and implemented in the research work reported herewith, are discussed next.

2.1 Equilibrium Local Magnetization

2.1.1 Hall Sensor Array

Due to magnetic flux quantization, the magnetic induction, B, at the surface of a superconducting sample is a direct measure of the vortex density $n_v = B/\Phi_\circ$. However, sample inhomogeneity due to variations in the doping and defect contents, the pinning-induced Bean profile, and the presence of a geometrical barrier spatially modulate the magnetic response of the sample. Therefore, a global magnetic measurement reflects only the average vortex density in the sample. Thermodynamic transitions, on the other hand, are driven by the local conditions. A spatially modulated density profile may result in coexistence of two phases, each with its own characteristic magnetization. The transition front that separates these phases propagates with scanning of an external parameter. Under such circumstances, a global sensor would smear out the sharp magnetic feature (for instance, discontinuous magnetization step of a first-order transition) that signals the phase transition.

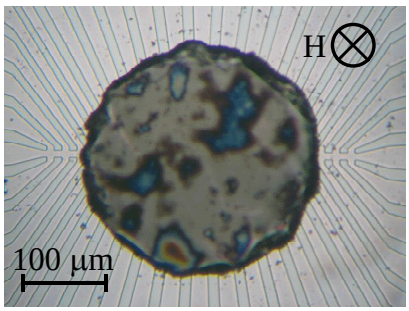

Fig. 2.1: *Disk shaped $Bi_2Sr_2CaCu_2O_8$ sample mounted on a Hall sensor array.*

This raises the need of magnetic sensors that can measure the magnetization locally

on the scale of the modulation. On the other hand, a single vortex resolution misses the thermodynamic collective behavior. We, therefore, employ a linear array of magnetic Hall sensors of 10×10 μm^2 each, which is much smaller than the typical sample size and much larger than both the size of a vortex ($\sim \lambda$) and the typical inter-vortex distances. In the Hall bar geometry, a Hall voltage is induced in a transverse direction to an applied electric current in the presence of magnetic field in the perpendicular direction $V_{Hall} = R_{Hall}IB$, by which the sample induction can be easily measured. The array is fabricated from a two-dimensional electron gas, trapped at the interface of a GaAs-AlGaAs heterostructure. We choose a relatively low carrier concentration of about 7×10^{11} electron/cm^2 to increase the Hall resistivity (R_{Hall} $\sim$0.1 Ω/G) while retaining a reasonably high mobility of 10^5 cm/Vsec. Using an extrinsically doped semiconductor results in a negligible temperature dependence of the Hall coefficient.

In normal operation mode the sample surface facing the sensors is cleaved and then mounted on top of the chip and fixed with grease under a microscope. A dc current of up to 400 μA is driven through the central channel, and the Hall voltage induced across each cross in the array is measured sequentially through a switcher. A sensitivity of 10 mG was obtained with a dc excitation, and of 1 mG in an ac mode.

2.1.2 Shaking

At low temperatures disorder plays a dominant role in the vortex thermodynamics, giving rise to various glassy phases. This is, however, reflected also in the vortex dynamics, in the form of a progressively slowed relaxation, that gives rise to hysteretic magnetization (see Sec. 1.4). The finite size of the sample also adds to that hysteresis (Sec. 1.7). The resulting hysteresis obscures the equilibrium ground state of the vortex system. In order to probe the thermodynamic phase diagram we applied 'shaking' - a vortex variant of a tapping technique [68, 21, 69]. It takes advantage of the layered structure of the material by using the short-range attractive interaction between inter-plane Josephson vortices and out-of-plane pancake vortex stacks within the crossing lattices configuration [13, 70]. By applying an in-plane ac field component, in addition to the out-of-plane dc one, Josephson vortices penetrate and leave the sample, while bisecting pancake stacks on their passage. These rare events occasionally agitate pancake vortices that are trapped away from their equilibrium position, and allow the pancake vortex matter to relax towards its equilibrium local density.

Typically an in-plane shaking field of 350 Oe amplitude and 10 Hz frequency was applied at low temperatures using superconducting X-Z coils, immersed inside the liquid

^{4}He dewar. The relevance of the in-plane field to the vortex thermodynamics in the out-of-plane direction is small due to the extreme material anisotropy. Nevertheless, an ac in-plane field does couple electromagnetically to the experimental setup that surrounds the sample, which demanded a careful design of the sample space on top of the mounting rod. One source of coupling is by excitation of eddy currents within metallic plates, such as the stainless steel cryostat. These currents partially screen the applied ac field on one hand, and produce heat on the other. Therefore, the sample space was built solely from insulating materials such as ceramics and G-10. The ac field attenuation within the cryostat double walls was measured to be on the order of 10%.

The second source of coupling is inductive, through open loops in the wiring of the device. This is usually reduced by twisting the 'high' and 'low' leads as to have a minimal cross-sectional area between them. However, the Hall bar geometry separates the highs and lows to opposite ends of the chip, as demonstrated schematically in the top view of Fig. 2.2(a). Using this bonding scheme, the pair of leads are twisted only outside the chip-holder, resulting in the several cm^2 pickup loop, shown in the side view, that encloses a large amount of flux. Therefore, in the revised design (Fig. 2.2(b)-top view) the chip is first mounted onto a sapphire plate with photolithographically defined metallic (Cr-Au) channels that short one constituent of a pair from the far side of the chip to the opposite side at which the other constituent resides. The resulting pickup loop has a ∼100 times smaller cross-sectional area (Fig. 2.2(b)-side view), and the actual pickup signal was attenuated by about 30 dB to less than 1 μV.

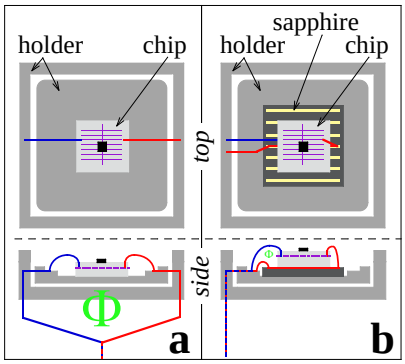

Fig. 2.2: *Top and side views of (a) The common sample space with a large pickup loop, and (b) the revised version with the sapphire plate that shrinks the pickup loop.*

An additional requirement of the setup is to minimize the projection of ac fields applied by the X-coil onto the out-of-plane direction. For that purpose the entire sample space was stretched by a spring onto two screws that can be manipulated from the rear end of the mounting rod. This allows rotation of the sample space by up to 5 degrees away from the axis of the rod in any desired direction. We then rotated the sample space at cold temperatures (but above T_c) as to minimize the ac Hall signal detected by the Hall sensors in the presence of a strong ac field applied by the X-coil. The extremely low pickup of our design enabled the alignment of the Hall-sensors plane to less than 0.01°. The actual angle between the axis of the X-coil and the sample is probably somewhat

larger, due to small misalignment between the surface of the chip and that of the cleaved sample. Nevertheless, the overall projection onto the out-of-plane direction is surely well below 1%.

2.2 Transport

2.2.1 Multi-terminal Measurements

The basic four-probe magneto-resistance measurement of a superconducting sample, in which current is driven between two external contacts and the voltage induced is measured on two internal contacts (see Fig. 2.3(a)), is indicative of the vortex phase [38, 71]. The quality of the contacts (Ohmic two-probe resistance lower than 10 Ω) dictates the measurement noise floor, typically not lower than $\sim 10^{-7}$ Ω. To achieve such a sensitivity we evaporate 2000 Å thick gold through a shadow mask on a freshly cleaved (or ion-milled) surface. 25 μm gold wires are than glued with silver-epoxy under a microscope to the gold contacts, and cured in an oven at 160°C for 2.5 hours. Their other ends are bonded with a ball-bonder. An ac lock-in technique is used for the actual measurement, where a low-noise transformer with turns ratio of 1:100 is used for impedance matching.

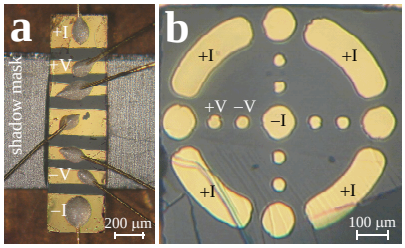

Fig. 2.3: *Contact geometries: (a) Four-probe measurement (sample bottom is glued to ion irradiation shadow mask). (b) Corbino disk.*

Naively, the measured resistivity should reflect the global flow characteristics of pancake vortices across the sample bulk, ρ_{ab}. In reality, the quantity measured in such a four-probe experiment is dominated by many other processes:

- Sample anisotropy - due to the layered structure of $Bi_2Sr_2CaCu_2O_8$, the measured resistance is dominated by the highly non-linear c-axis resistance.
- Edge barriers - below a certain temperature most of the current flows on the edges of the sample, thus probing the vortex flow at the edges and not in the bulk.
- Edge inductance - at lower temperatures the impedance of the sample edges is dominated by their geometrical inductance (this is one of the main findings, reported in detail in Sec. 3.3).

In order to extract the desired in-plane bulk resistance, these processes need to be identified, and their contributions eliminated.

The amount of current that penetrates across the sample thickness can be monitored in a flux-transformer measurement [62]. In this contact geometry, an identical set of contacts is prepared also on the opposite surface of the sample. For its measurement, one set of contacts is connected with silver-epoxy to matching evaporated Cr-Au contacts on the surface of a sapphire substrate in a flip-chip technique. The other set of contacts is wired in the usual manner. Such geometry allows to measure both the secondary voltage, induced at the bottom of the sample when injecting current from top, and the primary voltage measured at the top, and also the c-axis resistance alone.

As for the edge-related vortex mechanisms, one way of avoiding them is by employing the corbino-disk contact geometry (Fig. 2.3(b)). In it, current is injected radially. It exerts azimuthal force on the vortices, which thus flow in a circular path without ever crossing the sample edges. The induced voltage is also radial and is measured between additional sets of contacts at intermediate radii [72, 73].

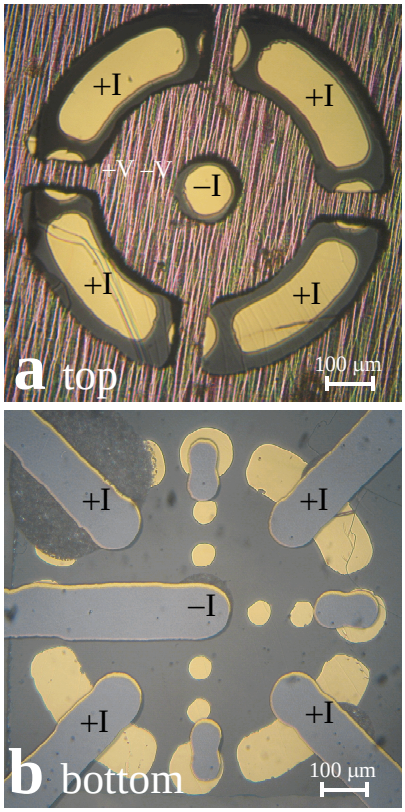

Fig. 2.4: *Double (flux-transformer) Corbino-disk with ion irradiated current contacts. (a) Top view: sample masked for irradiation. (b) Bottom view: flip-chip contact geometry.*

2.2.2 Current Contact Irradiation

In order to eliminate the c-axis contribution to the measured resistance we took advantage of the effect that heavy ion irradiation has on the vortex matter using a novel irradiation scheme. After preparing four-probe (or preferably flux-transformer eight-probe) contacts, we glue the ~ 20 μm thick sample with a droplet of crystalbond to a 38 μm thick stainless steel strip, that was cut with a guillotine to a width of 800-1000 μm. As shown in Fig. 2.3(a), the strip is placed between the external (current) contacts, but completely covers the central (voltage) contacts. The strip, with the sample glued beneath it, is then taped to a designated stage and shipped to the Grand Accélérateur National d'Ions Lourds (GANIL, Caen, France). There, it is irradiated with a high dose of 1 GeV Pb ions with a resulting matching field of 0.5 T. TRIM calculations for lead ions at such high energy give a stopping distance of 38.9 μm

in $Bi_2Sr_2CaCu_2O_8$, and 22.4 μm in stainless steel. Accordingly, the ions pass through the sample volume below the current contacts, leaving columnar defects along their tracks, but are stopped in the stainless steel, leaving the central region of the sample pristine. After irradiation the sample is removed from the strip with acetone and contacts are made in the usual procedure. Below the Bose-glass transition temperature (see Sec. 1.4), the vortices below the current contacts are trapped by the dense columnar defects, which greatly reduces ρ_c there. As a result, the current distributes evenly among the CuO_2 layers before it flows in the pristine central region. This allows to measure the induced voltage under uniform current distribution along the sample thickness.

Figure 2.4 shows a sample fabricated for conducting transport measurements under optimal conditions in a similar manner to a theoretical proposition [74]. The sample has the Corbino-disk contact geometry both on its upper surface (Fig. 2.3(b)), and on its bottom surface which is contacted to a sapphire substrate in a flip-chip technique (Fig. 2.4(b)). The central and circumferential current contacts of the sample were then ion irradiated through a matching shadow mask, as shown in Fig. 2.4(a). Consequently, below the Bose-glass transition transport measurement in this sample should be free of all the drawbacks mentioned above, thus allowing the direct measurement of the desired bulk ρ_{ab} induced by the vortex flow there. Unfortunately, measurements of these kind of samples are beyond the scope of this thesis.

2.3 Self-induced Field

2.3.1 Local Magnetization with Transport

A third type of measurement combines transport with local magnetization. As shown in Fig. 2.5, the array of Hall sensors, situated across the sample width, is used to measure a cross-section of the perpendicular component of the magnetic field self-induced by the transport current driven along the sample. A dc magnetic field and ac current are applied to distinguish between external and induced magnetic fields using a lock-in technique. The measured magnetic profile is then translated numerically via the inverse Biot-Savart law to the current distribution profile across the sample. A single central voltage contact is shorted to a single contact on the chip

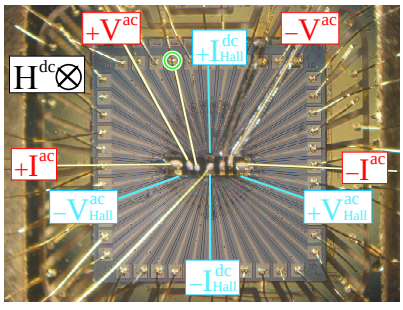

Fig. 2.5: *Contacted sample mounted on Hall sensor array for self-field measurement.*

(circled in Fig. 2.5) to eliminate gating of the two-dimensional electron gas by the sample, which would otherwise result in undesired variations of the Hall resistivity.

This method was employed before in a qualitative manner to study bulk versus edge flow patterns [67, 75], which result from the competition between bulk and edge energy barriers. In the current study we pursued this track, while gaining deeper understanding of the electrodynamics involved. It allowed us to render this method quantitative, and measure indirectly the actual resistances of the sample edges and the bulk below transport noise floor (reported in Sec. 3.3 and 3.4, respectively).

2.3.2 Local Magnetization with Flux-transformer

Finally, Fig. 2.6 shows a setup which allows simultaneous flux-transformer and self-field measurements. For its fabrication the chip was first coated in a photolithographic technique with a thin (less than 1 μm) layer of polyamide that serves as an electrically insulating buffer. Metallic (Cr-Al-Au) contacts were than evaporated on it through a shadow mask. UV glue was applied around these contacts and Ga-In eutectic droplets were placed on top of them under the microscope. The sample was then pressed against the wet surface inside a mask-aligner, followed by a short exposure of the chip and sample to UV light that cures the UV glue and fixes the sample to the chip. The upper surface of the sample is then contacted in the usual manner.

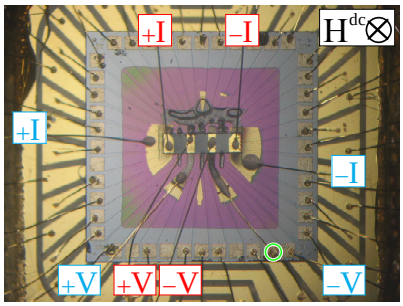

Fig. 2.6: *Flux-transformer configuration, flip-chip contacted on polyamide coated Hall sensor array.*

This delicate procedure yields an overall separation between the surface of the chip and the contacted bottom surface of the sample of less than 1 μm. It enables to study the way current distributes along the out-of-plane axis by comparing the self-induced magnetic profile measured at the surface of the sample to that measured one sample thickness away. Furthermore, when current is injected along the c-axis between top and bottom contacts (for e.g. between red and blue $+I$ contacts in Fig. 2.6) it first distributes across the upper planes, then tunnels through the layers, and eventually is collected by the contact at the bottom plane. This unique flow pattern is induced by the layered structure of $Bi_2Sr_2CaCu_2O_8$ that yields $\rho_c \gg \rho_{ab}$. Therefore, currents of opposite polarity flow on the top and bottom layers. In this scenario the Hall sensors measure the induced quantity $B_z(x, z+d) - B_z(x, z) \approx \partial B_z(x)/\partial z$. Using Maxwell's $\nabla \cdot \mathbf{B} = \partial B_z(x)/\partial z + \partial B_x(x)/\partial x = 0$

information can be inferred about the in-plane self-induced component $B_x(x)$. This is somewhat similar to the gradiometer device of Ref. [76] in which the $\partial B_z(x)/\partial z$ component of the sample dc magnetization was measured by a double-layer Hall sensor array.

2.4 Cryogenics

The cryogenic system (Fig. 2.7) is composed of a liquid helium flow cryostat for temperature stabilization and a superconducting magnet, both immersed inside a 110 liter helium storage dewar with a 3 inch wide neck. The cryostat is a homemade double-wall vessel with a needle valve, enabling controlled flow of liquid or gaseous helium into the sample space. The walls of the cryostat are vacuum-pumped before cooling to achieve thermal isolation. The flow of helium is facilitated by the pressure, generated within the dewar, which is maintained at about 5 psi by a back-pressure valve. Helium escaping the system is constantly transferred via recovery lines to the helium liquefying station.

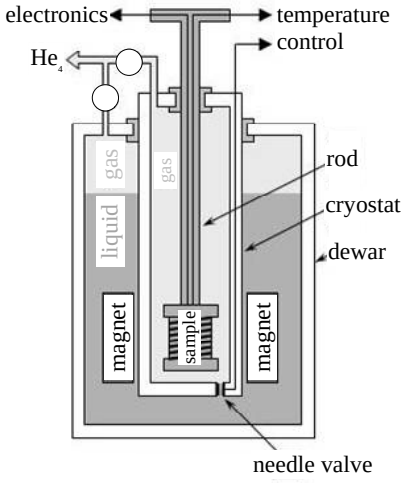

Fig. 2.7: *Setup.*

Temperature stabilization is achieved by careful control of the flow and of the temperature of the gas entering the sample space. The temperature is measured and stabilized using two temperature controllers: one in close proximity to the sample and the other at a heat exchanger copper block, located where the gas enters the cryostat. The temperature sensors used were factory-calibrated Lakeshore TG-120PL GaAs diodes. The diodes cover a 1.4 K-500 K range, have low magnetic field dependence, and require no periodic recalibration. The two 25 Ω heaters used for controlled heating were wound from NiCu 5 mil wires. For temperature control we used a Lakeshore 340 temperature controller.

3. Results

3.1 Thermodynamic Second-order Vortex Glass Transition

H. Beidenkopf, N. Avraham, Y. Myasoedov, H. Shtrikman, E. Zeldov, B. Rosenstein, E. H. Brandt and T. Tamegai "Equilibrium First-Order Melting and Second-Order Glass Transitions of the Vortex Matter in $Bi_2Sr_2CaCu_2O_8$". *Phys. Rev. Lett.* **95**, 257004 (2005).

We detected a novel thermodynamic glass transition of second-order in the vortex phase diagram of $Bi_2Sr_2CaCu_2O_8$. Numerous experimental results indeed indicated slowed vortex dynamics in $Bi_2Sr_2CaCu_2O_8$ at low temperatures. Most of these experiments studied the high-field part of the phase diagram above the melting line. This is mainly because the Bragg glass phase below it was commonly thought to be stable under thermal fluctuations. One of the features studied in this context was the irreversibility line that marks the onset of hysteretic magnetization. While the hysteresis is interlinked with the underlying bulk electrodynamics, it is affected by other mechanisms too (Sec. 1.7). In our study we relaxed the hysteretic magnetization of the vortex matter by applying an in-plane 'shaking' field. The resulting reversible magnetization revealed a sharp cusp marking a phase transition of second order. Moreover, a similar cusp was detected also below the melting line within the Bragg glass region of the phase diagram. This was the first indication of a thermodynamic transition underlying the dynamic irreversibility line, relating irreversibility to the onset of strong bulk pinning on approaching a thermodynamic glass transition. This transition was detected in all $Bi_2Sr_2CaCu_2O_8$ samples measured after its first identification. This result led to theoretical research regarding the novel transition. A similar transition was detected in an extensive computer simulation, predicting the thermally depinned ordered phase to have Ohmic resistance [77]. Theoretically, a thermodynamic glass transition, below which the replica symmetry of some order parameter is spontaneously broken, was subsequently derived both from the bare Ginzburg-Landau energy functional [78] as well as from an elastic description of the vortex system [79].

PRL 95, 257004 (2005) PHYSICAL REVIEW LETTERS week ending 16 DECEMBER 2005

Equilibrium First-Order Melting and Second-Order Glass Transitions of the Vortex Matter in $Bi_2Sr_2CaCu_2O_8$

H. Beidenkopf,[1,*] N. Avraham,[1] Y. Myasoedov,[1] H. Shtrikman,[1] E. Zeldov,[1] B. Rosenstein,[1,2] E. H. Brandt,[3] and T. Tamegai[4]

[1]*Department of Condensed Matter Physics, Weizmann Institute of Science, Rehovot 76100, Israel*
[2]*National Center for Theoretical Sciences and Electrophysics Department, National Chiao Tung University, Hsinchu 30050, Taiwan, Republic of China*
[3]*Max-Planck-Institut für Metallforschung, Heisenbergstrasse 3, D-70506 Stuttgart, Germany*
[4]*Department of Applied Physics, The University of Tokyo, Hongo, Bunkyo-ku, Tokyo 113-8656, Japan*

(Received 16 July 2005; published 16 December 2005)

The thermodynamic H-T phase diagram of $Bi_2Sr_2CaCu_2O_8$ was mapped by measuring local *equilibrium* magnetization $M(H, T)$ in the presence of vortex shaking. Two equally sharp first-order magnetization steps are revealed in a single temperature sweep, manifesting a liquid-solid-liquid sequence. In addition, a second-order glass transition line is revealed by a sharp break in the equilibrium $M(T)$ slope. The first- and second-order lines intersect at intermediate temperatures, suggesting the existence of four phases: Bragg glass and vortex crystal at low fields, glass and liquid at higher fields.

DOI: 10.1103/PhysRevLett.95.257004 PACS numbers: 74.25.Qt, 64.70.Pf, 74.25.Dw, 74.72.Hs

The magnetic field vs temperature (H-T) phase diagram of the vortex matter in high-temperature superconductors, and in $Bi_2Sr_2CaCu_2O_8$ (BSCCO), in particular, has drawn extensive scientific attention [1]. The commonly cited thermodynamic phase diagram of BSCCO currently consists of a single unified first-order (FO) melting line. It separates the low-field quasi-long-range ordered Bragg glass (BrG) phase from the high-field liquid and glass phases [1–6]. It is not clear, however, whether the two high-field disordered phases are thermodynamically distinct, or rather reflect a gradual dynamic crossover from liquid into a frozen, pinned state upon cooling [7,8]. In this Letter we show that the equilibrium phase diagram of the vortex matter is indeed more diverse than the one usually considered.

Experimentally, one of the main obstacles in mapping the low-temperature thermodynamics of the vortex matter is its logarithmically slow relaxation rate. Consequently, the phase diagram has been studied in the past mostly through dynamic phenomena. Two prime examples are the irreversibility line itself, marking the onset of hysteresis, and the second magnetization peak (SMP), observed along such hysteretic magnetization loops [9].

Recently, though, vortex shaking was shown to be extremely effective in catalyzing relaxation at low temperatures [2,10,11]. Its application unveiled the inverse melting and the thermodynamic FO transition as the phenomenon underlying the nonequilibrium SMP [2]. The shaking method employs the segregated penetration of an in-plane field component into the highly anisotropic BSCCO samples in the form of Josephson vortices, which are confined in between the CuO_2 planes. In the presence of an *ac* in-plane field, the Josephson vortices instantaneously bisect the pancake vortex (PV) stacks on their passage, interacting mainly with adjacent PVs, while most of the PVs in the stack remain at rest [12]. These occasional interactions agitate pinned PVs, assisting them in assuming their equilibrium configuration.

Within the present study we performed local magnetization measurements by field and temperature sweeps, while utilizing the shaking method, to map the *equilibrium* phase diagram of the vortex matter. The cross mapping of the FO melting line along both sweeping directions shows an excellent agreement. Temperature sweeps provided particularly sharp features, with which we demonstrate a liquid-solid-liquid sequence of phases. Ertaş and Nelson have predicted such a liquid-solid-liquid sequence to occur within a single temperature sweep [13], but it was never observed experimentally. We further find evidence of a novel second-order (SO) phase transition within the vortex solid phase, which bears important consequences regarding the nature of the BrG phase.

The reported results were obtained with a slightly overdoped BSCCO crystal with $T_c \approx 90$ K grown by the traveling solvent floating zone method [14]. This specific sample was polished into a triangular prism of base $660 \times 270\ \mu m^2$ and height 70 μm [15] (other samples yielded similar results, to be presented elsewhere). The sample was attached onto an array of eleven $10 \times 10\ \mu m^2$ GaAs/AlGaAs Hall sensors. In all measurements taken below 60 K the sample was subject to a 10 Hz in-plane *ac* field of amplitude 350 Oe, which was aligned parallel to the planes to an accuracy of a few millidegrees. Note that according to the anisotropic scaling theory [1] this in-plane field is effectively attenuated by a factor $\gamma \simeq 200$—the anisotropy constant in BSCCO. We found that at higher temperatures shaking had no effect on the FO transition besides a small broadening (see below).

The field sweep mapping of the FO melting line is shown in Fig. 1. The collapse of the hysteretic magnetiza-

PRL **95,** 257004 (2005) PHYSICAL REVIEW LETTERS week ending 16 DECEMBER 2005

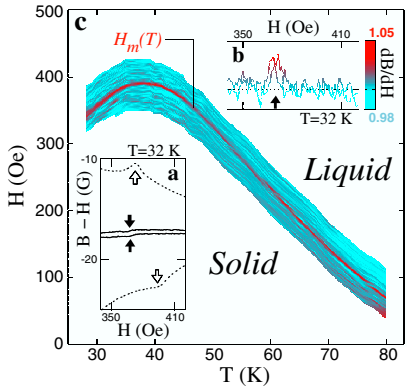

FIG. 1 (color online). (a) The 32 K field sweeps with (solid curve) and without (dotted curve) an in-plane 350 Oe-10 Hz shaking field. Reversible steps in magnetization (solid arrows) appear instead of the hysteretic SMP (open arrows) upon shaking. (b) The derivative of the induction with respect to applied field dB/dH at 32 K as a color scheme. The first-order transition appears as a paramagnetic peak on top of the $dB/dH \approx 1$ background. (c) Successive mapping of the first-order melting line $H_m(T)$ measured by field sweeps.

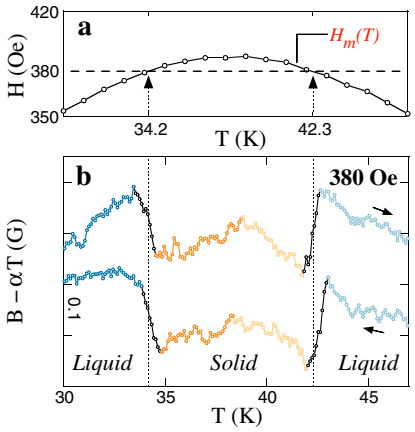

FIG. 2 (color online). (a) The FO melting line $H_m(T)$ mapped via field sweeps (open circles). (b) Local induction $B(T)$ in the presence of shaking, measured upon temperature sweep at 380 Oe along the dashed line in (a). A linear slope αT was subtracted for clarity. The two equally narrow FO magnetization steps (black segments) show a liquid-solid-liquid sequence. The temperatures at which the phase transitions occur coincide with those, extracted from field sweeps (doted lines). The color code reflects different phases in Fig. 4.

tion into a reversible behavior upon shaking is demonstrated in Fig. 1(a) taken at 32 K. A reversible magnetization step appears instead of the SMP. To better resolve the step we plot in Fig. 1(b) the derivative of the measured induction with respect to applied field dB/dH. The FO transition thus appears reversibly as a δ-like peak on top of the $dB/dH \approx 1$ background. Figure 1(c) shows a color scheme of the derivatives dB/dH measured by field sweeps within the temperature range 28–80 K. The individual melting peaks combine to give the locus of the FO transition line $H_m(T)$. Its negative slope at elevated temperatures becomes positive below 38 K. This nonmonotonic behavior marks the change in the character of the transition from thermally induced above the extremum to disorder driven in the inverse-melting region [5,6,13].

In addition to the field sweeps, our experimental setup also enables temperature sweeps in the presence of vortex shaking. It thus allows one to measure directly the temperature dependence of the equilibrium magnetization at a constant applied c-axis field. At fields slightly lower than 390 Oe [e.g., at 380 Oe along the dashed line in Fig. 2(a)] these sweeps should cross the melting line twice. Remarkably, the measured local induction in Fig. 2(b) indeed shows two very clear and opposite equilibrium magnetization steps on both descending and ascending sweeps. Note that for clarity we have subtracted from the data a linear slope αT. It is contributed both by the slight temperature dependence of the Hall coefficients of the sensors and by the linear term of the magnitude of the diamagnetic equilibrium magnetization, which monotonically decreases with temperature. This is the first observation of two FO transitions obtained in a single temperature sweep. Moreover, the two steps are equally sharp and with comparable heights of about 0.15 G. This demonstrates that the thermally and disorder-driven processes, responsible for the melting and the inverse melting, respectively, are equivalent mechanisms leading to a FO destruction of the quasiordered vortex solid.

The temperatures at which the magnetization steps appear along the temperature sweep of Fig. 2(b) are in complete agreement with the melting behavior deduced from field sweeps (dotted lines). Therefore, the transition line in Fig. 2(a) is independent of the specific H-T path along which it is approached—a mandatory equilibrium property. The remaining small hysteresis of 0.1 to 0.2 G between downward and upward sweeps apparently results from surface barrier effects, while the vortices in the bulk are well equilibrated by the shaking. The finite widths (about 0.7 K) that the melting steps attain are mainly due to a spatial and a temporal averaging mechanisms. The first is introduced by the sensor's finite active area that averages over the propagating melting front [16], which results from the spatially inhomogeneous equilibrium magnetization profile [17]. The temporal one is a by-product of the shaking technique. The in-plane field component is known to slightly reduce the melting temperature [12,18,19]. Consequently, our time averaged measurement in the presence of the ac in-plane shaking field results in an additional broadening due to the instantaneous periodic shift of the effective local melting temperature.

We thus turn to report the detection of a novel phase transition, whose signature is a distinct break in the slope of the magnetization $M(T)$. It is visible around 37 K in Fig. 2(b) at 380 Oe, and becomes much more pronounced

PRL **95,** 257004 (2005) PHYSICAL REVIEW LETTERS week ending 16 DECEMBER 2005

at fields further away from the extremum of the FO melting line, as depicted by Fig. 3. The 420 Oe temperature sweep [Fig. 3(a)] does not intersect with the FO line, hence no steps appear in the local induction. Nevertheless, a sharp break in slope is clearly resolved along both descending and ascending temperature sweeps at T_g. A sharp reversible break in the induction slope appears also in the 350 Oe temperature sweep of Fig. 3(b) (dotted line) in between the two melting steps, hence within the solid phase. This nonanalytic behavior is emphasized by the sharp step in the derivative dB/dT shown in the insets. These kinks were found also in other samples and at various Hall-sensor locations, and did not depend on the sweeping rate. We thus conclude that this break in slope of the equilibrium magnetization $M(T)$ indicates a thermodynamic SO phase transition.

Mapping of both the first-order $H_m(T)$ and second-order $H_g(T)$ transition lines onto the equilibrium H-T phase diagram is given in Fig. 4. The SO line (solid dots) intersects the melting curve (open circles) and shows weak field dependence throughout the mapped region (and therefore cannot be readily observed by field sweeps). The resulting phase diagram consists of *four* distinct thermodynamic phases.

The high-field part of the novel SO line can be naturally identified with the long sought glass transition line. It asserts that the low-temperature glass phase is indeed thermodynamically distinct from the high-temperature liquid one. Several experimental studies have observed bulk irreversibility features in BSCCO, which appeared above $H_m(T)$ at about 35 K [20,21]. However, all these studies probed dynamic or nonequilibrium vortex properties. The glass line of Fig. 4 is the first experimental evidence of such a thermodynamic transition in BSCCO.

Yet, the most intriguing result in Fig. 4 is the detection of the SO line within the vortex solid region. This implies that two distinct thermodynamic phases are present in the low-field region below $H_m(T)$, contrary to the common belief that a single BrG phase prevails throughout this part of the phase diagram. A number of previous studies indicated a depinning line of similar topology within the BrG below $H_m(T)$ [20]. However, all these measurements probed only the nonequilibrium properties, which were consistent with the existing theoretical dynamic predictions and simulations of depinning [13,22]. In contrast, the present finding of a thermodynamic line requires a more fundamental reconsideration.

It is interesting to note that in $YBa_2Cu_3O_7$ crystals a thermodynamic signature of a SO transition within the liquid phase has been reported [23]. There, however, the SO line emanates from the upper critical point of the FO line, directly extending it to higher fields. This topology is consistent with several dynamic measurements in $YBa_2Cu_3O_7$ [24,25], although alternative topologies have been also suggested [26,27]. In contrast, our thermodynamic data of BSCCO show that the SO and the FO transitions are two independent lines that intersect each other nearly at a right angle.

Several theoretical studies have shown that under the elastic medium approximation quasi-long-range order of the vortex lattice is still retained in the presence of quenched disorder, giving rise to the BrG phase [28,29]. This phase was found to be stable at all temperatures (as long as topological excitations are excluded) in systems of dimensionality greater than two and lower than four. This is probably the reason why a nontopological thermodynamic phase transition of the BrG phase was hardly ever considered in 3D models. An exception is a Josephson-glass line that was suggested to exist within the BrG region [30]. Still, the general belief is that the BrG phase is robust until dislocations proliferate, which gives rise to the FO phase transition [6,8,28]. In 2D systems, however, the BrG models did find a possible finite-temperature depinning

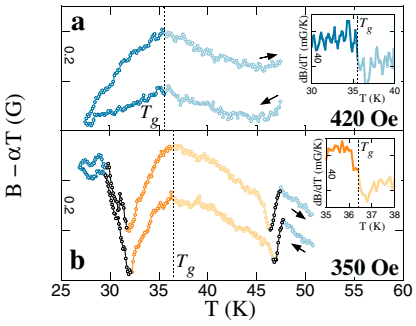

FIG. 3 (color online). Local induction $B(T)$, measured along temperature sweeps while shaking. A reversible sharp break in the slope (at the dotted lines) appears both above [(a) 420 Oe] and below [(b) 350 Oe] the melting line $H_m(T)$. The insets show a corresponding step in the derivative dB/dT, signifying a thermodynamic second-order phase transition.

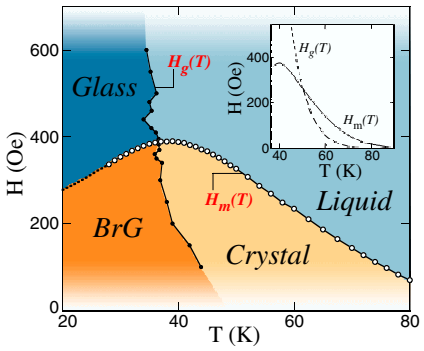

FIG. 4 (color online). The thermodynamic phase diagram of BSCCO accommodates *four* distinct phases, separated by a first-order melting line $H_m(T)$ (open circles), which is intersected by the second-order glass line $H_g(T)$ (solid dots). The inset plots an equivalent phase diagram, calculated based on Ref. [31], consisting of a second-order replica symmetry breaking lines $H_g(T)$ both above (dotted line) and below (dashed line) the first-order transition $H_m(T)$ (solid line).

transition, above which disorder is no longer relevant. Therefore, the observed SO transition could be accounted for within these models only in the extreme case of vanishing coupling between the superconducting layers.

In contrast, in a recent theoretical work [31] the free energy of the vortex matter in the presence of quenched disorder was explicitly calculated under the lowest-Landau-level approximation in a 3D model. It was found that two transitions are present: a FO melting, at which the quasi-long-range order is destroyed, and a SO glass transition, below which the replica symmetry is spontaneously broken. The inset of Fig. 4 shows the phase diagram, calculated using a similar effective 2D model with parameters optimized for BSCCO [32]. The calculations reproduce the measured features very well. Amongst them are the melting and inverse-melting behavior, the discontinuity of the magnetization slope dM/dT at the glass transition, and the $H_g(T)$ line itself, which resides at slightly higher temperatures as compared to experiment. In addition, the calculations show that the portions of the $H_g(T)$ line, lying above and below the FO transition $H_m(T)$ (dotted and dashed lines, respectively), are slightly shifted from each other. Therefore, they do not cross the melting line at a single point, but rather form two closely located tricritical points along it. This minute shift can hardly be seen in the inset of Fig. 4 and is below our current experimental resolution.

Within this model the high-field glass phase and the low-field BrG are strongly pinned and replica symmetry broken, whereas the two high-temperature phases are replica symmetric and thus reversible. This conclusion of reversibility is consistent also with the existing dynamic measurements [20]. It is therefore tempting to speculate that the phase above $H_g(T)$ and below $H_m(T)$ should acquire a true crystalline order. However, since Rosenstein and Li did not calculate the structure factor and our measurements do not probe this quantity, the proposed vortex crystal phase certainly calls for further experimental and theoretical investigations.

In summary, we present thermodynamic evidence of a possibly second-order glass transition line that splits the quasiordered vortex solid into two distinct phases. By comparing the results with existing dynamic measurements and a new theoretical study, we suggest that the two phases are BrG and a vortex crystal. The glass line crosses the first-order melting line near its extremum and extends to higher fields, giving rise to two thermodynamically distinct disordered phases—a glass and a liquid.

We thank D. Li, V. M. Vinokur, and B. Horovitz for stimulating discussions. This work was supported by the Israel Science Foundation Center of Excellence, by the German-Israeli Foundation G. I. F., by the Minerva Foundation, Germany, and by Grant-in-aid for Scientific Research from the Ministry of Education, Culture, Sports, Science, and Technology, Japan. B. R. acknowledges the support of the Albert Einstein Minerva Center for Theoretical Physics and E. Z. the U.S.-Israel Binational Science Foundation (BSF).

*Electronic address: haim.beidenkopf@weizmann.ac.il

[1] G. Blatter and V. B. Geshkenbein, *The Physics of Superconductors* (Springer, New York, 2003), Vol. I, Chap. 10, p. 725.
[2] N. Avraham *et al.*, Nature (London) **411**, 451 (2001).
[3] Y. Radzyner, A. Shaulov, and Y. Yeshurun, Phys. Rev. B **65**, 100513(R) (2002).
[4] V. Vinokur *et al.*, Physica (Amsterdam) **295C**, 209 (1998).
[5] G. P. Mikitik and E. H. Brandt, Phys. Rev. B **68**, 054509 (2003); J. Kierfeld and V. Vinokur, Phys. Rev. B **69**, 024501 (2004).
[6] T. Giamarchi and S. Bhattacharya, *High Magnetic Fields: Applications in Condensed Matter Physics, Spectroscopy* (Springer, New York, 2002), p. 314.
[7] C. Reichhardt, A. van Otterlo, and G. T. Zimányi, Phys. Rev. Lett. **84**, 1994 (2000).
[8] Y. Nonomura and X. Hu, Phys. Rev. Lett. **86**, 5140 (2001); P. Olsson and S. Teitel, Phys. Rev. Lett. **87**, 137001 (2001).
[9] B. Khaykovich *et al.*, Phys. Rev. Lett. **76**, 2555 (1996).
[10] M. Willemin *et al.*, Phys. Rev. Lett. **81**, 4236 (1998).
[11] G. P. Mikitik and E. H. Brandt, Phys. Rev. B **69**, 134521 (2004).
[12] A. E. Koshelev, Phys. Rev. Lett. **83**, 187 (1999).
[13] D. Ertaş and D. R. Nelson, Physica (Amsterdam) **272C**, 79 (1996).
[14] N. Motohira *et al.*, J. Ceram. Soc. Jpn. Int. **97**, 994 (1989).
[15] D. Majer, E. Zeldov, and M. Konczykowski, Phys. Rev. Lett. **75**, 1166 (1995).
[16] A. Soibel *et al.*, Nature (London) **406**, 282 (2000).
[17] E. Zeldov *et al.*, Phys. Rev. Lett. **73**, 1428 (1994).
[18] S. Ooi *et al.*, Phys. Rev. Lett. **82**, 4308 (1999).
[19] B. Schmidt *et al.*, Phys. Rev. B **55**, R8705 (1997).
[20] D. T. Fuchs *et al.*, Phys. Rev. Lett. **80**, 4971 (1998); C. D. Dewhurst and R. A. Doyle, Phys. Rev. B **56**, 10 832 (1997); Y. Yamaguchi *et al.*, Phys. Rev. B **63**, 014504 (2001); S. Ooi, T. Mochiku, and K. Hirata, Physica (Amsterdam) **378C**, 523 (2002); Y. Matsuda *et al.*, Phys. Rev. Lett. **78**, 1972 (1997); S. Ooi, T. Shibaushi, and T. Tamegai, Physica (Amsterdam) **284B**, 775 (2000).
[21] T. Shibauchi *et al.*, Phys. Rev. Lett. **83**, 1010 (1999).
[22] R. Sugano *et al.*, Physica (Amsterdam) **357C**, 428 (2001).
[23] F. Bouquet *et al.*, Nature (London) **411**, 448 (2001).
[24] H. Safar *et al.*, Phys. Rev. Lett. **70**, 3800 (1993).
[25] W. K. Kwok *et al.*, Phys. Rev. Lett. **84**, 3706 (2000).
[26] K. Shibata *et al.*, Phys. Rev. B **66**, 214518 (2002).
[27] B. J. Taylor *et al.*, Phys. Rev. B **68**, 054523 (2003).
[28] T. Giamarchi and P. LeDoussal, Phys. Rev. B **52**, 1242 (1995).
[29] T. Nattermann, Phys. Rev. Lett. **64**, 2454 (1990).
[30] B. Horovitz and T. R. Goldin, Phys. Rev. Lett. **80**, 1734 (1998); B. Horovitz, Phys. Rev. B **72**, 024519 (2005).
[31] D. Li and B. Rosenstein, Phys. Rev. Lett. **90**, 167004 (2003); cond-mat/0411096.
[32] B. Rosenstein and D. Li (unpublished).

3.2 Anisotropy Scaling of the Glass Transition

H. Beidenkopf, T. Verdene, Y. Myasoedov, H. Shtrikman, E. Zeldov, B. Rosenstein, D. Li and T. Tamegai "Interplay of Anisotropy and Disorder in the Doping-Dependent Melting and Glass Transitions of Vortices in $Bi_2Sr_2CaCu_2O_{8+\delta}$". *Phys. Rev. Lett.* **97**, 167004 (2007).

To further characterize the extended vortex phase diagram consisting of a first-order melting transition and a second-order glass transitions, we studied the dependence of these transition lines on the oxygen over-doping of the sample, δ. The main effect of oxygen over-doping is to increase the coupling between the superconducting layers. This stiffens the pancake vortex stacks, thereby reducing the sample anisotropy and enhancing the elasticity of the vortex matter [6, 80, 81, 82]. In addition, the excess oxygen atoms serve as added point defects [83]. We found that the glass transition obeys a surprisingly simple anisotropy-scaling law which neglects the effect of disorder altogether [84, 85]. By fitting the doping-dependent phase diagrams to those calculated from a theoretical model [78], we found that although defect density is known to increase with over-doping, the disorder strength decreases. This was attributed to the reduced anisotropy, which renormalizes the disorder strength and decreases it.

In view of the reported results, we attempted to study the dependence of the phase diagram on disorder content alone without varying the sample anisotropy. The defect density can be varied by bombarding the sample with light elements, such as electrons [27, 20] or protons [28, 29]. We thus irradiated a ~ 20 μm thick $Bi_2Sr_2CaCu_2O_8$ sample with protons at 2.25 MeV with total fluency of 1×10^{16} p/cm^2 in the Van der Graph accelerator at the Weizmann Institute. TRIM calculation yields a stopping distance of 38.4 μm. Unlike electrons, which are known to induce only point-like de-

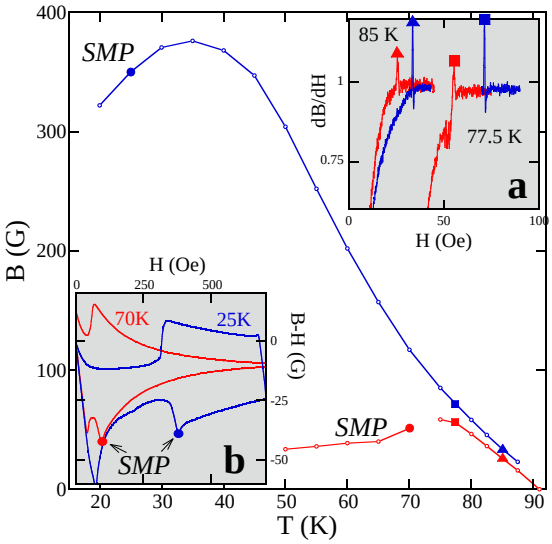

Fig. 3.1: *Melting line before (blue) and after (red) irradiating the sample with protons. (a) ac-susceptibility melting peaks. (b) Second magnetization peaks.*

fects on their passage through the sample, collisions of the heavier protons also result in a negligible concentration of defect cascades which may introduce some c-axis correlations [86, 87].

The preliminary results obtained thus far indicate an enormous enhancement of disorder strength, which we believe to originate mainly from uncorrelated point-like defects. At the highest temperatures, at which the melting transition is induced by thermal fluctuations, the effect of proton irradiation is negligible, as in the case of electron irradiation [20]. Figure 3.1(a) shows that the paramagnetic melting peaks detected in ac-susceptibility measurements retain their shape, indicative of the underlying first-order transition [88], and merely shift to slightly lower vortex densities. However, the maximum of the melting line (Fig. 3.1), below which it becomes disorder induced, shifts from 35 K to the unprecedented high temperature of 75 K after irradiation, restricting the ordered region of the phase diagram to extremely low vortex densities. The dynamic second magnetization peak (SMP), a signature of the inverse melting transition [21] which is commonly observed below 40 K in pristine samples, is accordingly detected in the hysteretic magnetization at 70 K (Fig. 3.1(b)). While this feature is typical to pristine samples with point-like defects, it is absent in heavily ion irradiated samples with correlated pinning centers [89], which signifies the dominance of point-like defects over the cascades in inducing the observed behavior in the proton irradiated sample. These preliminary results emphasize the potential in systematically studying the complete vortex phase diagram, including its second-order glass transition, in proton-irradiated samples.

PRL 98, 167004 (2007) PHYSICAL REVIEW LETTERS week ending 20 APRIL 2007

Interplay of Anisotropy and Disorder in the Doping-Dependent Melting and Glass Transitions of Vortices in $Bi_2Sr_2CaCu_2O_{8+\delta}$

H. Beidenkopf,[1,*] T. Verdene,[1] Y. Myasoedov,[1] H. Shtrikman,[1] E. Zeldov,[1] B. Rosenstein,[2] D. Li,[3] and T. Tamegai[4]

[1]*Department of Condensed Matter Physics, Weizmann Institute of Science, Rehovot 76100, Israel*

[2]*Electrophysics Department, National Chiao Tung University, Hsinchu 30050, Taiwan, Republic of China*

[3]*Department of Physics, Peking University, Beijing 100871, China*

[4]*Department of Applied Physics, The University of Tokyo, Hongo, Bunkyo-ku, Tokyo 113-8656, Japan*

(Received 23 September 2006; published 20 April 2007)

We study the oxygen doping dependence of the equilibrium first-order melting and second-order glass transitions of vortices in $Bi_2Sr_2CaCu_2O_{8+\delta}$. Doping affects both anisotropy and disorder. Anisotropy scaling is shown to collapse the melting lines only where thermal fluctuations are dominant. Yet, in the region where disorder breaks that scaling, the glass lines are still collapsed. A quantitative fit to melting and replica symmetry-breaking lines of a 2D Ginzburg-Landau model further reveals that disorder amplitude weakens with doping, but to a lesser degree than thermal fluctuations, enhancing the relative role of disorder.

DOI: 10.1103/PhysRevLett.98.167004 PACS numbers: 74.25.Dw, 64.70.Pf, 74.25.Qt, 74.72.Hs

Elasticity, thermal energy, disorder, and interlayer coupling are some of the closely competing energy scales in the intricate H-T phase diagram of the vortex matter in the layered high-temperature superconductor $Bi_2Sr_2CaCu_2O_{8+\delta}$ (BSCCO) [1–6]. The low-temperature part of the equilibrium phase diagram of BSCCO was recently made accessible to experiment by vortex shaking [7–9]. It unveiled a first-order (FO) inverse-melting line, which continues the thermal melting line from high temperatures [8] separating low-field ordered phases from high-field amorphous ones. A second-order (SO) transition line, at which low-temperature glassy phases get thermally depinned, was subsequently reported [9]. In this Letter we study the oxygen doping dependence of these transition lines. We show that the SO line scales with material anisotropy even where the FO line does not, and that effective disorder weakens with doping, but gains relative dominance over thermal fluctuations.

We present measurements of optimally doped (OPD), slightly overdoped (SOD), overdoped (OVD), and highly overdoped (HOD) BSCCO crystals [10,11] with critical temperatures $T_c = 92$, 90, 88.5, and 86 K, respectively, corresponding to hole concentrations of 0.171, 0.180, 0.184, and 0.190 [12]. Various crystal geometries were studied with typical sizes of $\sim 300 \times 300 \times 40\ \mu m^3$. They were mounted on $10 \times 10\ \mu m^2$ Hall sensor arrays, fabricated in a GaAs/AlGaAs heterostructure. At low temperatures we utilized a 350 Oe in-plane ac shaking field of 10 Hz to relax the pancake vortices toward their equilibrium configuration [7–9]. Conjugating local probes with shaking yielded the equilibrium reversible magnetization of the samples.

Figure 1 shows the local induction $B(H, T)$ measured in the SOD sample by sweeping the temperature T at a constant out-of-plane field H in the presence of an in-plane shaking field. A linear term $\alpha_H T + \beta_H$ was subtracted from each temperature sweep [Fig. 1(a)] to flatten the originally increasing ($\alpha_H > 0$) local induction. As a result, the FO and SO singular behavior can be readily traced throughout the H-T phase diagram.

The FO melting transition is manifested by a discontinuous step in the magnetization along the dash-dotted line in Fig. 1. It separates the high-field amorphous glass and liquid phases from the low-field quasi-long-range–ordered Bragg glass (BrG) [5,13]. The melting line becomes nonmonotonic at a certain temperature [8,9]. Its inverse-melting part is believed to be an order-disorder

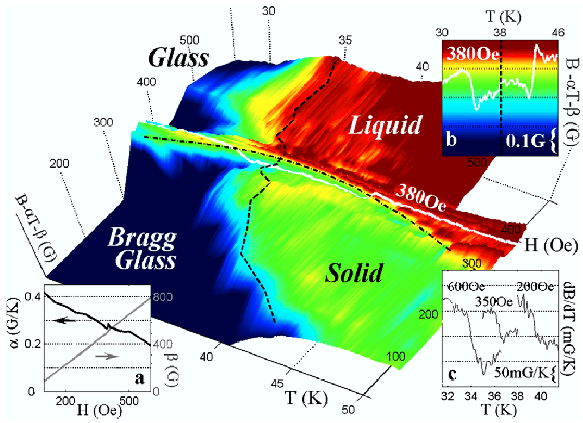

FIG. 1 (color online). The local induction shows FO (dash-dotted line) and SO (dashed line) transition lines in the H-T phase diagram. The induction in the high-temperature depinned liquid and solid phases was artificially flattened by a linear subtraction $\alpha_H T + \beta_H$ (hence the constant color). The low-temperature BrG and glassy phases have thus a finite positive slope. (a) Values of α_H and β_H used. (b) FO-SO-FO transition sequence at a 380 Oe temperature sweep on the background of the color bar. (c) Discontinuous steps in dB/dT, manifesting the SO nature of the transition.

PRL 98, 167004 (2007) PHYSICAL REVIEW LETTERS week ending 20 APRIL 2007

transition, induced mainly by quenched disorder and not by thermal fluctuations [1–5,14–16].

The SO phase transition is manifested by a break in the slope of the magnetization at T_g, marked in Fig. 1 by the dashed line. It separates the fully flattened high-temperature magnetization ($dB/dT|_{T>T_g} - \alpha \approx 0$) of constant color from a low-temperature region of nonzero slope ($dB/dT|_{T<T_g} - \alpha > 0$), whose color varies with temperature. The nonanalyticity at T_g is demonstrated in Fig. 1(c), which shows ~40 mG/K steps in dB/dT for temperature sweeps lying below as well as above the FO line. The location of the SO line above melting resembles earlier dynamic irreversibility measurements [17–21] and theoretical models of a glass transition [1–5,22–24]. Few dynamic measurements found a similar line of thermal depinning below melting [9,25–30], which separates the BrG phase below it from a thermally depinned solid, whose detailed characteristics are not yet certain.

We mapped three more samples of various doping levels that yielded the B-T phase diagram plotted in Fig. 2. The melting line shifts as a whole to higher fields with doping due to the decrease in anisotropy, which implies stronger interlayer coupling and higher stiffness of the pancake vortex stacks [10,30–32]. As the FO line shifts to higher fields, its maximum shifts toward increasingly higher temperatures (inset of Fig. 2). Identifying these maxima with the crossover from disorder to thermally dominated behavior [1–5] may suggest that doping enhances disorder. The SO transition line also shifts upward, further signifying that disorder is enhanced with doping. However, we will show below that this conclusion is inaccurate. Moreover, arguing naively that the balance between characteristic energies constrains the SO line to bisect the FO one at its maximum [1] is also too simplistic. The inset of Fig. 2 clearly shows that in overdoped samples the bisection point resides below the FO maximum temperature (the overlap of the two in the OPD sample is apparently accidental). Therefore, a naive description of thermal depinning cannot account for both the SO line and the FO maximum behavior (for instance, the latter is directly affected also by elasticity) [2–4].

We now present a quantitative scaling analysis of the doping dependence, parameterized by the sample anisotropy ratio $\varepsilon^2 = m_{ab}/m_c$ (m_i is the electronic effective mass in the ith direction). For high-κ superconductors, such as BSCCO, the Ginzburg-Landau (GL) free energy functional can be recast into an isotropic ($\varepsilon = 1$) form by rescaling its parameters [33]. We focus on one such transformation [34] that rescales space, magnetic induction, the penetration depth λ_0, and the coherence length ξ_0. Models for high-temperature melting are usually independent of ξ_0, and find λ_0 to enter with some model-dependent power as a proportionality factor. For definiteness we resort to a specific model [6,35] for a FO evaporation line with no disorder from vortex solid to pancake gas $B_E(t) \propto (\varepsilon^2/\lambda_0^2 d)(1 - t^2)/t$, where $t = T/T_c$ and d is the interplane separation. The scaling transformation [34] indeed renders $B_E(t)$ isotropic.

Figure 3 shows the rescaled FO and SO lines. The high-temperature parts of the FO lines are perfectly collapsed by dividing their induction axes by a constant [30]. $B_E(t)$ (dash-dotted line) fits the collapsed melting lines precisely, asserting that the multiplicands in this procedure are $(\varepsilon_\circ/\varepsilon)^2$, normalized by the OPD $\varepsilon_\circ^{-1} \approx 500$ [36]. Anisotropy scaling collapses the data down to $t_{\rm th} \approx 0.58$. Below $t_{\rm th}$, which appears to be independent of anisotropy, the rescaled FO lines disperse again, and the fit to $B_E(t)$ breaks. The flattening of the FO line towards an inverse-melting behavior results from quenched disorder, which

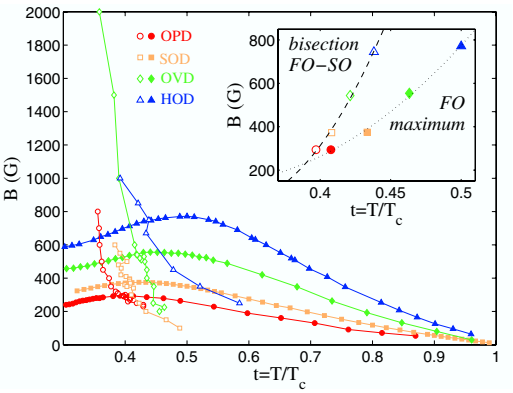

FIG. 2 (color online). FO and SO transition lines (solid symbols and open symbols, respectively) measured with OPD (○), SOD (□), OVD (◇), and HOD (△) samples. The inset shows the doping dependence of the maximum of the FO line and its bisection with the SO line. Dotted and dashed lines are second-degree polynomial fits.

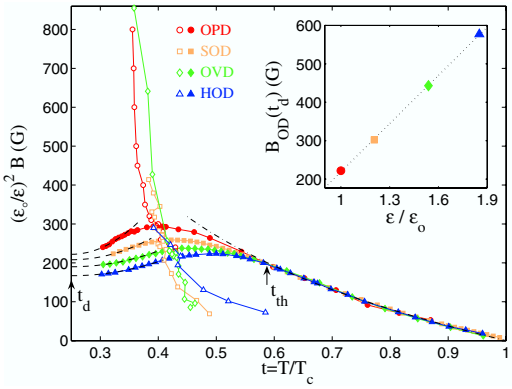

FIG. 3 (color online). Data collapse of the overdoped high-temperature ($t > t_{\rm th}$) FO lines (solid symbols) onto the OPD line, which also collapses the SO lines (open symbols). The fit to $B_E(t)$ (dash-dotted) sets the anisotropy ratios $\varepsilon/\varepsilon_\circ$ to 1, 1.20, 1.54, and 1.85 for the OPD (○), SOD (□), OVD (◇), and HOD (△) samples, respectively. The inset shows the linear dependence of the characteristic $B_{\rm OD}(t_d)$ on $\varepsilon/\varepsilon_\circ$ (dotted line).

PRL 98, 167004 (2007) PHYSICAL REVIEW LETTERS week ending 20 APRIL 2007

gains dominance with decreasing temperatures [1]. Accordingly, above $t_{\rm th}$ the FO transition is purely thermally induced, and completely unaffected by disorder [14]. Just below $t_{\rm th}$ disorder becomes a relevant, though not yet a dominant, energy scale.

This counterparts the extremely low-temperature behavior, where thermal energy becomes negligible relative to pinning, resulting in a flat temperature-independent behavior of the FO lines [1]. Indeed the FO lines in Fig. 3 tend to flatten toward their ends, below which 350 Oe 10 Hz shaking is insufficient for detecting a reversible melting step. We thus conjectured a similar doping-independent threshold temperature $t_d \approx 0.25$, below which thermal energy becomes irrelevant. We fitted the low-temperature order-disorder lines by a leading order expansion $B_{\rm OD}(t \gtrsim t_d) \sim B_{\rm OD}(t_d) + \Lambda(t - t_d)^2$, which agrees very well with measurement. We can, therefore, estimate $B_{\rm OD}(t_d)$, at which elasticity is balanced solely by the disordering potential. It increases monotonically with doping (inset of Fig. 3), stating that with reducing anisotropy elasticity gains dominance also over disorder.

Yet, the most remarkable outcome of the anisotropy scaling shown in Fig. 3 is the simultaneous collapse of the SO transition lines (with zero freedom). The SO lines reside in a temperature region where anisotropy scaling of the melting lines fails due to effects of disorder. Still, the same scaling transformation somehow succeeds in rendering the glass transition isotropic, even though this transition is believed to be intimately related with the competition between disorder and thermal fluctuations.

To gain deeper understanding of the low-temperature behavior, we fit the measured transition lines to those predicted by a recent calculation [37], which gives access to the doping dependence of the model's free parameters. It incorporates thermal, disordering, and elastic energies to yield bisecting FO and SO lines. The pancake vortex system is modeled by the 2D GL theory. We interpret this single layer model as the outcome of an integration of all other layers out of a complete 3D theory, resulting in an effective 2D model whose renormalized coefficients may still depend on anisotropy ε of a 3D mass tensor.

The free energy functional is averaged over Gaussian disorder in the coefficients of the quadratic and quartic terms using the replica method. Taking the lowest-Landau-level (LLL) approximation yields for the replicated partition function

$$\overline{Z^n} = \int_{\Psi_1 \ldots \Psi_n} \exp\Big(-\sum_a G_0(\Psi_a) + \sum_{a,b} \tilde{R}\,|\Psi_a|^2 |\Psi_b|^2\Big),$$

$$G_0(\Psi) = \int \frac{d^2x}{4\pi}\Big(a_T|\Psi|^2 + \frac{|\Psi|^4}{2} + \frac{\kappa^2(b-h)^2}{\pi\sqrt{2{\rm Gi}}bt}\Big),$$

where $\tilde{R} = a_T^2 bR/32\pi^2$, R is the disorder amplitude in the coefficient of the quadratic LLL term, $b = B/\tilde{H}_{c2}$, $a_T = (b + t - 1)/(2\pi^2 b^2 t^2 {\rm Gi})^{1/4}$ is the LLL parameter, Gi is the effective Ginzburg number that generally scales thermal fluctuations, and κ is the GL parameter. Randomness in the coefficient of the quartic LLL term, although crucial for obtaining the nonanalyticity of SO, has negligible effect on the locus of the transition lines, and is therefore neglected in the present context.

The FO line is calculated by equating the energies of the homogeneous and crystalline states under the influence of disorder in Gaussian approximation. This extends beyond the earlier calculation, which treated disorder perturbatively [38]. The glass line is found from the stability analysis of the replica symmetric solution. The replica symmetry breaking (RSB) is continuous. The corresponding Parisi function describing the hierarchial structure of the glassy state and its detailed derivation can be found in Ref. [37].

The model's free parameters are R, Gi, $\tilde{T}_c$, and $\tilde{H}_{c2} = T_c(dH_{c2}/dT)|_{T_c}$. However, due to a hidden symmetry, given by ${\rm Gi}/\tilde{H}_{c2}^2$ and ${\rm Gi}/R^2$, the theory effectively has only three independent fitting parameters. We therefore fixed $\tilde{H}_{c2} = 100$ T, for simplicity, consistent with our limited range of hole concentrations [12]. Figure 4 presents two fitting strategies motivated by different physical behaviors. The first (thick lines) is optimized to fit the collapsed parts of the phase diagram—SO lines and FO ones for $t > t_{\rm th}$. Interestingly, this set simultaneously provides a collapsed FO line also for $t < t_{\rm th}$. This results from the above symmetry of the model in which Gi and ε take the same role, defining a relation $R \propto \sqrt{\rm Gi}$ along which the calculated phase diagram remains unchanged under anisotropy rescaling. The thick lines in the insets of Fig. 4 show the resulting parameters ${\rm Gi} = 3.91(\varepsilon_0/\varepsilon - 0.37)^2$ and $R = 1.54(\varepsilon_0/\varepsilon - 0.37)$. The departure of the calculated FO line from the measured ones below $t_{\rm th}$ may indicate that theory lacks a symmetry-breaking mechanism once anisotropy scaling breaks in experiment.

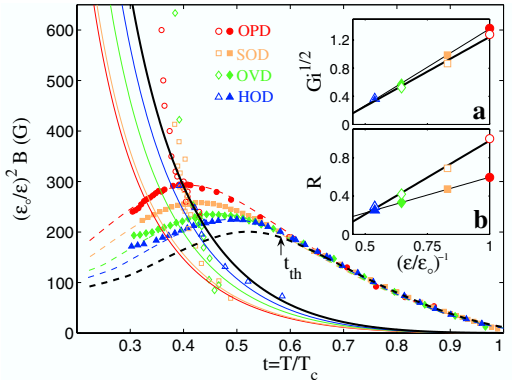

FIG. 4 (color online). Fits of FO (dashed) and SO (solid) lines of the LLL 2D GL model with $\tilde{H}_{c2} = 100$ T, $\tilde{T}_c = 103, 101, 98$, and 95 K for the OPD (○), SOD (□), OVD (◇), and HOD (△) samples, respectively. The values of Gi (a) and R (b) were fixed either by fitting the SO lines and FO ones above $t_{\rm th}$ (thick lines) or by fitting the full FO lines (thin lines).

An alternative fit (thin lines), faithful to the complete FO lines, dictates the slightly different set of values $\mathrm{Gi} = 4.77(\varepsilon_\circ/\varepsilon - 0.38)^2$, $R = 0.75(\varepsilon_\circ/\varepsilon - 0.2)$ (insets, thin lines). The excellent fit of the FO lines (dashed line) suggests that the effective 2D model still captures the essential physics involved. Its validity should break down at very low temperatures, where indeed it misses the flattening of the FO lines as t_d is approached, and close to T_c due to critical fluctuations, which may explain the 10% overestimate in the fitted bare $\tilde{T}_c$ values [39]. Substituting this set of values in the calculation of the RSB lines (solid lines) with zero freedom also produces a good fit that improves with doping, but misses the anisotropy rescaling of the measured SO lines. Nevertheless, the discrepancy between the two sets of values of the different fitting strategies is small, and vanishes in the high doping limit.

In Fig. 4(a) the reduced dominance of thermal fluctuations with doping is clearly captured by the decrease in Gi. Its dependence on anisotropy is closer to the 3D $1/\varepsilon^2$ than to the 2D ε-independent behavior. Remarkably, the disorder amplitude in Fig. 4(b) also decreases with doping. This contrasts the result of Ref. [40], which found that oxygen addition increases the defects concentration. The apparent contradiction is resolved by noting that the disorder amplitude is affected also by the anisotropy dependence of the effective pinning potential, which decreases with doping as the vortex stacks get stiffer. The overall decrease of R suggests that the latter mechanism is dominant, not the rising defect concentration.

Last, while both Gi and R decrease with doping, Gi has a stronger dependence on anisotropy. This clarifies the true mechanism that shifts the maximum of the FO line and its bisection with the SO line toward higher temperatures with doping (Fig. 2). Although the magnitude of the disorder amplitude decreases with increased doping, disorder still gains relative dominance over thermal fluctuations, which decrease faster with ε.

In summary, ε^2 scaling accounts for the reduced anisotropy of BSCCO samples with doping down to t_{th}. Below t_{th}, where disorder becomes relevant, ε^2 scaling still collapses the SO lines. From the quantitative agreement with the LLL 2D GL model, we deduce that disorder and thermal fluctuations weaken relative to elasticity with increased doping, which shifts the FO line toward higher fields. Disorder still gains relative dominance over thermal fluctuations, which concurrently shifts the maximum of the FO line and its bisection with the SO line towards higher temperatures.

We thank V. M. Vinokur and G. P. Mikitik for stimulating discussions. This work was supported by the Israel Science Foundation Center of Excellence, by the German-Israeli Foundation G.I.F., by Grant-in-aid for Scientific Research from the Ministry of Education, Culture, Sports, Science, and Technology, Japan, by the National Science Foundation of China, and by the MOE ATU Program of R.O.C. NSC952112M009048. B. R. acknowledges the support of the Albert Einstein Minerva Center for Theoretical Physics, and E. Z. the US-Israel Binational Science Foundation (BSF).

*Electronic address: haim.beidenkopf@weizmann.ac.il

[1] D. Ertas and D. R. Nelson, Physica (Amsterdam) **272C**, 79 (1996).
[2] G. P. Mikitik and E. H. Brandt, Phys. Rev. B **68**, 054509 (2003).
[3] J. Kierfeld and V. Vinokur, Phys. Rev. B **69**, 024501 (2004).
[4] V. Vinokur *et al.*, Physica (Amsterdam) **295C**, 209 (1998).
[5] T. Giamarchi and P. LeDoussal, Phys. Rev. B **55**, 6577 (1997).
[6] L. I. Glazman and A. E. Koshelev, Phys. Rev. B **43**, 2835 (1991).
[7] M. Willemin *et al.*, Phys. Rev. Lett. **81**, 4236 (1998).
[8] N. Avraham *et al.*, Nature (London) **411**, 451 (2001).
[9] H. Beidenkopf *et al.*, Phys. Rev. Lett. **95**, 257004 (2005).
[10] S. Ooi, T. Shibauchi, and T. Tamegai, Physica (Amsterdam) **302C**, 339 (1998).
[11] N. Motohira *et al.*, J. Ceram. Soc. Jpn. Int. Ed. **97**, 994 (1989).
[12] G. C. Kim *et al.*, Phys. Rev. B **72**, 064525 (2005).
[13] E. Zeldov *et al.*, Nature (London) **375**, 373 (1995).
[14] B. Khaykovich *et al.*, Phys. Rev. B **56**, R517 (1997).
[15] Y. Radzyner, A. Shaulov, and Y. Yeshurun, Phys. Rev. B **65**, 100513 (2002).
[16] P. Olsson and S. Teitel, Phys. Rev. Lett. **87**, 137001 (2001).
[17] R. Cubitt *et al.*, Nature (London) **365**, 407 (1993).
[18] E. Zeldov *et al.*, Europhys. Lett. **30**, 367 (1995).
[19] M. Konczykowski *et al.*, Physica (Amsterdam) **332C**, 219 (2000).
[20] M. B. Gaifullin *et al.*, Phys. Rev. Lett. **84**, 2945 (2000).
[21] F. Portier *et al.*, Phys. Rev. B **66**, 140511(R) (2002).
[22] Y. Nonomura and X. Hu, Phys. Rev. Lett. **86**, 5140 (2001).
[23] S. Ryu, A. Kapitulnik, and S. Doniach, Phys. Rev. Lett. **77**, 2300 (1996).
[24] J. P. Rodriguez, Phys. Rev. B **73**, 214520 (2006).
[25] D. T. Fuchs *et al.*, Phys. Rev. Lett. **80**, 4971 (1998).
[26] C. D. Dewhurst and R. A. Doyle, Phys. Rev. B **56**, 10 832 (1997).
[27] Y. Matsuda *et al.*, Phys. Rev. Lett. **78**, 1972 (1997).
[28] S. Ooi, T. Mochiku, and K. Hirata, Physica (Amsterdam) **378C**, 523 (2002).
[29] R. Sugano *et al.*, Physica (Amsterdam) **388C**, 637 (2003).
[30] Y. Yamaguchi *et al.*, Phys. Rev. B **63**, 014504 (2000).
[31] B. Khaykovich *et al.*, Phys. Rev. Lett. **76**, 2555 (1996).
[32] T. Hanaguri *et al.*, Physica (Amsterdam) **256C**, 111 (1996).
[33] G. Blatter, V. B. Geshkenbein, and A. I. Larkin, Phys. Rev. Lett. **68**, 875 (1992).
[34] R. A. Klemm and J. R. Clem, Phys. Rev. B **21**, 1868 (1980).
[35] L. L. Daemen *et al.*, Phys. Rev. Lett. **70**, 1167 (1993).
[36] M. Tokunaga *et al.*, Phys. Rev. B **67**, 134501 (2003).
[37] D. Li, B. Rosenstein, and V. Vinokur, J. Supercond. Novel Mag. **19**, 369 (2007).
[38] D. Li and B. Rosenstein, Phys. Rev. Lett. **90**, 167004 (2003).
[39] A. I. Larkin and A. Varlamov, *Theory of Fluctuations in Superconductors* (Oxford, England, 2005), Chap. 2.
[40] T. W. Li *et al.*, Physica (Amsterdam) **257C**, 179 (1996).

3.3 Transport Properties Governed by the Edge Inductance

H. Beidenkopf, Y. Myasoedov, E. Zeldov, E.H. Brandt, G.P. Mikitik, T. Tamegai, T. Sasagawa and C. J. van der Beek "Transport Properties Governed by the Inductance of the Edges in $Bi_2Sr_2CaCu_2O_8$". *submitted to Phys. Rev. Lett.*

We studied the dynamical aspects of the thermodynamic phase diagram. As discussed in Sec. 1.6 and 1.7, the sample edges and extreme anisotropy due to its layered structure render naive transport measurement inadequate. We thus devised an alternative indirect approach, which combines measurement of the current distribution within the sample [67] with a simple, but apparently accurate, model of the sample edges and bulk in terms of electrodynamic components - resistors and inductors [90]. In this chapter, this method is applied first to unveil the true electrodynamic edge mechanism that drives the previously unresolved T_x transition [47]. We show that this is the temperature below which the edge inductance governs the transport properties of the sample, and indicate the associated vortex flow characteristics. The edge inductance is then used as a probe for measuring the edge resistance far below typical transport noise. In the next chapter, we show that a similar electrodynamic transition takes place in the bulk, and then use it to probe the bulk resistance on approaching the novel glass transition.

A different possible approach, comprising of a Corbino-disk contact geometry with ion-irradiated current contacts, was put forward in Sec. 2.2.2. However, the quenched disorder in the sample, which result in exponentially decreasing resistance with temperature, restricts its application to relatively high temperatures, before the typical transport noise floor is reached.

Transport Properties Governed by the Inductance of the Edges in $Bi_2Sr_2CaCu_2O_8$

H. Beidenkopf,[1,*] Y. Myasoedov,[1] E. Zeldov,[1] E.H. Brandt,[2]
G.P. Mikitik,[2,3] T. Tamegai,[4] T. Sasagawa,[5] and C. J. van der Beek[6]

[1]*Department of Condensed Matter Physics, Weizmann Institute of Science, Rehovot 76100, Israel*
[2]*Max-Planck-Institut für Metallforschung, Heisenbergstr. 3, D-70506 Stuttgart, Germany*
[3]*B. Verkin Institute for Low temperature Physics & Engineering, Kharkov 61103, Ukraine*
[4]*Department of Applied Physics, The University of Tokyo, Hongo, Bunkyo-ku, Tokyo 113-8656, Japan*
[5]*Materials and Structures Laboratory, Tokyo Institute of Technology, Kanagawa 226-8503, Japan*
[6]*Laboratoire des Solides Irradiées, CNRS UMR 7642 & CEA/IRAMIS/DRECAM, Ecole Polytechnique, 91128 Palaiseau cedex, France*

(Dated: June 25, 2009)

We study the distribution of transport current across superconducting $Bi_2Sr_2CaCu_2O_8$ crystals and the vortex flow through the sample edges. We show that the T_x transition is of electrodynamic rather than thermodynamic nature, below which vortex dynamics is governed by the edge inductance instead of the resistance. This allows measurement of the resistance down to two orders of magnitude below the transport noise. By irradiating the current contacts the resistive step at vortex melting is shown to be due to loss of c-axis correlations rather than breakdown of quasi-long-range order within the a-b planes.

PACS numbers: 74.25.Dw, 74.25.Bt, 74.25.Fy, 74.72.Hs

Numerous phase transitions have been proposed to interpret the intricate $B-T$ phase diagram of vortex matter in the high temperature superconductor $Bi_2Sr_2CaCu_2O_8$ (BSCCO) [1, 2]. The first-order melting at T_m, that separates a quasi-ordered vortex solid from a vortex liquid, is widely accepted to be a genuine thermodynamic phase transition [3, 4]. Experiments indicate that the glass line, T_g, is another thermodynamic transition that apparently separates amorphous solid from liquid at high fields [5–8] and Bragg glass from depinned lattice at low fields [7, 8]. On the other hand, the T_x transition, which resides above T_m and T_g, has remained highly controversial. A number of experiments [9–14], numerical simulations [15, 16], and theoretical studies [17, 18] argued that it is a transition into a phase with intermediate degree of order such as a disentangled liquid [19] or a decoupled- [20, 21], soft- [22], or super-solid [23, 24]. In this letter we show that T_x does not represent a thermodynamic transformation of a bulk vortex property, but rather reflects an *electrodynamic* crossover in the dynamic response of the sample *edges*. The inductance of the sample edges, though immeasurably low, completely governs the vortex dynamics below T_x. We use this finding to investigate the resistance due to vortex motion down to two orders of magnitude below the sensitivity of transport measurements.

The resistance of several BSCCO single crystals of typical size $1500\times350\times20$ μm^3 in a dc magnetic field, $H_{dc}\|$c-axis, was measured using two complimentary techniques: directly via transport and indirectly by determining the ac current distribution with Biot-Savart law from the self-induced ac magnetic field profile using an array of 10×10 μm^2 GaAs Hall sensors. In addition, to eliminate the c-axis contribution to the measured resistance we irradi-

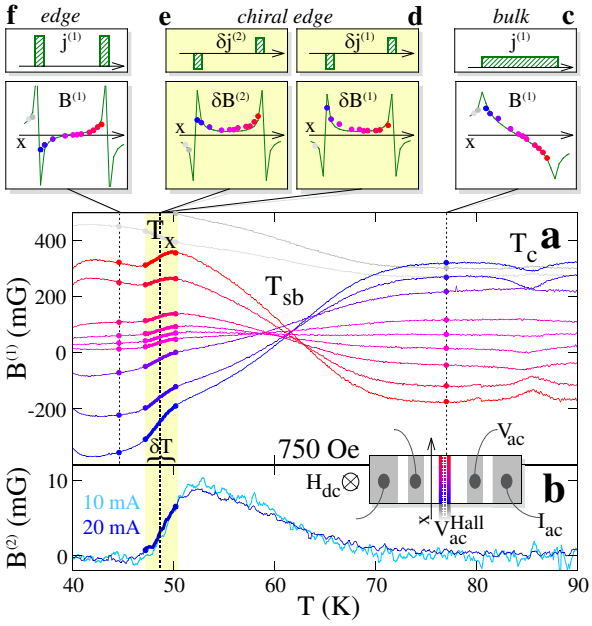

FIG. 1: (color online) Hall sensor array measurement of the ac magnetic field self-induced by a 15 mA, 73 Hz ac current in BSCCO crystal A. (a) First-harmonics of individual sensors. (b) Second-harmonics from a sensor close to the edge at two current amplitudes normalized to 10 mA. (c-f) Magnetic profiles measured (•) and calculated (solid lines) from current profiles (upper panels) using the Biot-Savart law: (c) Uniform bulk flow at high temperatures turns to (f) edge flow at low temperatures. Chiral edge flow vanishes at T_x from (d) first- and (e) second-harmonics. Inset in (b): Schematic location of Hall sensors relative to the contacted sample.

ated the current contacts at GANIL (Caen, France) with 1 GeV Pb ions to a matching dose of $B_\Phi = 0.5$ T, while masking the rest of the sample, which remained pristine.

Figure 1(a) shows the temperature dependence of the current-induced ac field, $B^{(1)}(x)$. At high temperatures the current distributes uniformly because it is solely dictated by the flux flow resistance in the bulk, $R_b(T)$. Accordingly, $B^{(1)}(x)$ measured by the Hall sensors across the sample (Fig. 1(c), circles) fits perfectly to that calculated via Biot-Savart law (solid line) from a uniform current $j^{(1)}(x)$ (upper panel).

With cooling $B^{(1)}(x)$ gradually flattens out, becomes completely flat at T_{sb}, and eventually inverted at yet lower temperatures. The inverted $B^{(1)}(x)$ profile is associated with essentially pure edge currents (Fig. 1(f)). The Bean-Livingston surface barrier [25] and the platelet sample geometry [26] impose an energetic barrier that progressively impedes vortex passage through the edges. This defines an effective edge resistance, $R_e(T)$, that decreases rapidly with cooling and becomes smaller than the bulk resistance $R_b(T)$ below T_{sb}. As a result, most of the current shifts from the bulk, where little force is required to move vortices across, towards the edges, where it facilitates the hindered vortex entry and exit [27]. Bulk vortex pinning becomes dominant only at significantly lower temperature (not shown).

The dynamic properties of the surface barriers have two types of asymmetries. The first arises from the two edges of the sample generally having somewhat different microscopic imperfections. It leads to different edge resistances and therefore asymmetric current distribution between the right and left edges. The T_x line, situated below T_{sb} (Fig. 2), marks the temperature below which this right-left asymmetry sharply disappears and the amplitudes of the two edge currents become equal (Fig. 1(f)). Hence, an antisymmetric current component $\delta j^{(1)}$ (Fig. 1(d)), that was present above T_x, and its induced small symmetric contribution $\delta B^{(1)}(x) = B^{(1)}(x, T_x + \frac{\delta T}{2}) - B^{(1)}(x, T_x - \frac{\delta T}{2})$ to the otherwise antisymmetric $B^{(1)}(x)$, vanish below T_x.

The second type of asymmetry arises from the inherent asymmetry between hard vortex entry and easy exit through the surface barriers [28]. Since the vortex entry and exit sides swap during the ac cycle, this asymmetry gives rise to a unique chiral second harmonic edge current, $\delta j^{(2)}$, and to the corresponding second harmonic signal $\delta B^{(2)}(x)$ (Fig. 1(e)). It builds up gradually upon cooling (Fig. 1(b)) until it pinches off sharply at T_x (hereinafter determined at half of the $B^{(2)}(x)$ roll-off). Accordingly, T_x marks the temperature below which the vortex flow turns insensitive to both the entry-exit and the right-left asymmetries of the surface barriers.

The T_x transition was previously ascribed to the advent of a new vortex phase with a higher degree of order [9, 15–18]. We show that T_x has rather electrodynamic nature, arising from the sample edges inductance. Following Ref. [29] we model the vortex dynamics by equivalent electric circuit with three parallel channels - the bulk and two edges. Our measurements show no dependence on the current magnitude (Fig. 1(b), dark vs. pale lines). Therefore, we follow the Ohmic model of Ref. [29] that assigns each channel geometrical self and mutual inductances in series to their resistances.

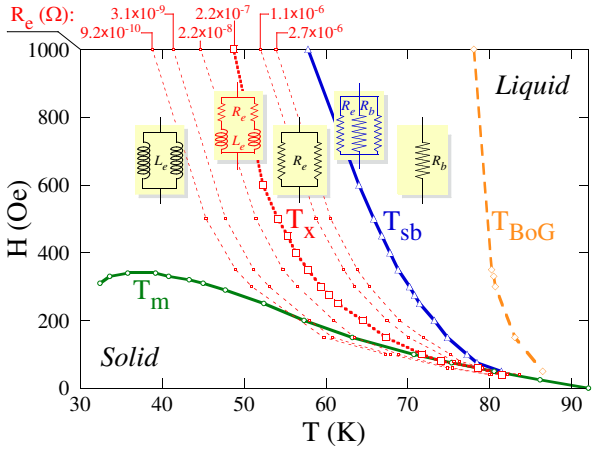

FIG. 2: (color online) High temperature phase diagram of the vortex matter in BSCCO crystal B. T_m is the first-order melting (○). Below T_{sb} (△) the edges shunt most of the current from the bulk, while below the frequency dependent T_x (□) the edge impedance becomes predominantly inductive. Ion irradiated regions exhibit the Bose Glass transition, $T_{\rm BoG}$ (◇), below which vortices are pinned to columnar defects. The dotted lines represent equal edge-resistance contours extracted from the frequency and field dependence of T_x.

The sample inductance is usually disregarded since it is immeasurably small in direct transport measurements. Nevertheless, it affects the current distribution in the sample. The effective edge inductance, as opposed to the edge resistance, is temperature independent and dictated solely by the geometry of the edges $L_e = (\mu_0/4\pi)l[\ln(2w/d) + 1/4]$, where l, w, and d are the sample's length, width, and thickness, respectively [29]. T_x is the temperature below which the edge impedance turns from being predominantly resistive to inductive, $R_e(T_x) = 2\pi f L_e$. Consequently, T_x is frequency dependent and allows sensitive determination of $R_e(T)$ similar to the extraction of resistance from ac susceptibility [30, 31]. At 350 Oe and $f = 73$ Hz we measure $T_x \simeq 59$ K. Using $L_e = 304$ pH, calculated from sample geometry, we obtain $R_e(59\ \text{K}) = 1.4 \times 10^{-7}\Omega$ (Fig. 3, white cross). Note, that this value is 2-3 orders of magnitude lower than the current dependent resistance measured simultaneously in transport (open circles), which below T_{sb} should reflect the edge resistance R_e.

The transport resistance measured in the geometry of Fig. 3(a), however, has a large contribution from the c-

axis resistivity, ρ_c. Due to the extreme anisotropy of BSCCO ρ_c is orders of magnitude larger than ρ_{ab}, giving rise to nonlinearities and shear effects [32, 33]. The dissipation due to ρ_c that arises from current tunneling between the CuO_2 planes, however, is not accounted in the electrodynamic considerations of the edge inductance [29]. The non-uniformity of current flow along the c-axis can be remedied by introducing columnar defects solely under the current contacts (see Fig. 3(b)). Below the Bose-glass transition, $T_{\rm BoG}$ (Fig. 2, diamonds), the vortices become strongly pinned to the columnar defects increasing the c-axis correlations and greatly reducing the sample anisotropy [34–36]. This is remarkably demonstrated in a multi-contact measurement of a sample irradiated in such a manner (Fig. 3(c)). Above $T_{\rm BoG}$ the high anisotropy results in poor c-axis current penetration. Therefore, the primary resistance, R_p, measured on the current injecting surface, is much higher than the secondary resistance, R_s, measured on the opposite surface. At $T_{\rm BoG}$, signaled by the plunging c-axis resistance R_c, the secondary resistance recovers and equals the primary [37, 38]. After current contact irradiation the resistance, measured by voltage contacts in the central pristine region of the sample (Fig. 3, open squares), decreases by two orders of magnitude, and turns Ohmic. Moreover, the resistive behavior now becomes fully consistent with the inductive edge model. As shown below, all the data sets can be fitted by a single parameter - an effective edge inductance of L_e =490 pH (black cross in Fig. 3). The similarity of this value to the calculated 304 pH is remarkable, considering the crude modeling of the edges (round wires of diameter d [29]) and the uncertainties in various parameters.

To further establish the role of the edge inductance in the T_x transition we extract $R_e(T,H)$ by repeatedly monitoring the current distribution with frequencies ranging from 0.3 Hz to 1 kHz. At all frequencies $B^{(2)}$ rises gradually with cooling (Fig. 4(a)), as more current is shunted to the edges, until it vanishes at a frequency-dependent temperature, $T_x(f)$. The extracted edge resistance, $2\pi f L_e$ versus $T_x(f,H)$ (Fig. 4(b), circles), matches accurately the resistance measured in transport (thin lines), and extrapolates it well below the transport noise floor. A fit to an Arrhenius behavior (dotted line) yields an edge energy barrier $U_e^o \sim 18T_c$.

The excellent agreement of the edge resistance extracted from $T_x(f)$ to that measured in transport confirms that the edge inductance drives the electrodynamic T_x transition. In terms of vortex dynamics, the resistive component of the edge impedance arises from vortex dissipation thermally activated over the surface barriers. Dissipation due to bulk vortex motion is negligible, since bulk pinning is very weak, hence $R_b \gg R_e$. Nevertheless, bulk redistribution of vortices reflects the inductive component of the edge impedance. With changing current polarity during the ac cycle the vortices, complying

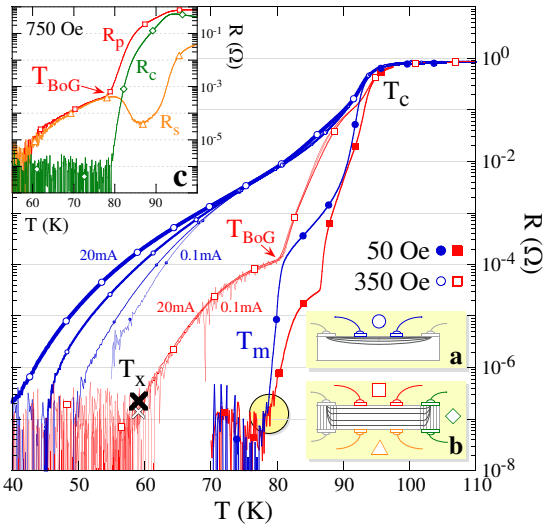

FIG. 3: (color online) The pristine transport resistance (BSCCO crystal B) is non-Ohmic (shrinking ○: I_{ac} =20, 5, 1, 0.1 mA, 73 Hz) due to non-uniform current flow along c-axis (inset a). After contact irradiation (□) and below $T_{\rm BoG}$ as the current penetrates uniformly (inset b) the resistance turns Ohmic and matches that extracted from T_x (×). Below the resistive step at T_m the pristine (●) and irradiated (■) resistances are equal. Inset c: Multi-contact measurement of a current-contact-irradiated sample (b). At low fields and below $T_{\rm BoG}$, signaled by the vanishing c-axis resistance (◇), current distributes uniformly across the sample thickness, and the secondary resistance (△) equals the primary one (□).

with the $B^{(1)}(x)$ profile of Fig. 1(f), shift from one side of the sample to the opposite in association with an inductive dB/dt. At high temperatures the number of vortices redistributing from right to left during half a cycle due to $dB^{(1)}(x)/dt$ is still much smaller than those that dissipatively cross the edges and move across the sample. With cooling, however, the number of vortices that cross the edges decreases exponentially. Below T_x it becomes negligible compared to the number of redistributing vortices. The second harmonic vanishes because vortex redistribution in a 'closed box' is necessarily antisymmetric. Our main finding is that although the edge inductance is immeasurably small in transport measurements, it completely governs vortex dynamics below T_x.

We now focus on the behavior of the edge resistance at melting. In the pristine sample a sharp resistive drop [39] is observed at T_m (Fig. 3, solid dots), whereas after contact irradiation the behavior is continuous (solid squares). Moreover, the two curves merge at the lowest measurable resistance (circled), indicating that in the presence of a uniform c-axis current the edge resistance shows no sharp features. Hence, the common resistive melting drop in BSCCO arises from a sharp drop in ρ_c.

Another intriguing feature at melting (Fig. 4(c), as-

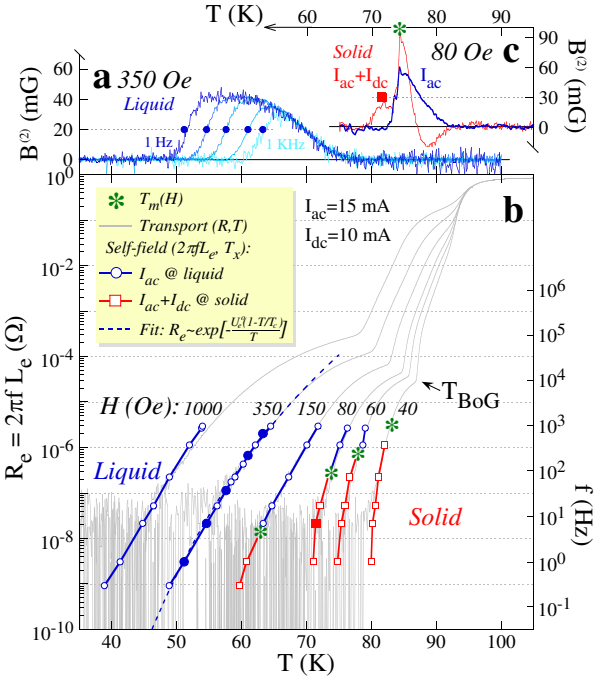

FIG. 4: (color online) (a) Second-harmonic signals showing the frequency dependence of T_x (•). (b) It enables to extract the temperature dependent edge resistance (○) which is thermally activated (dashed) and accurately matches the measured transport resistance (thin lines). Below melting (∗) a small dc bias is required to extract the edge resistance (□). (c) This is seen in the second-harmonic signal (thick line) that vanishes at melting (∗) but recovers with bias (thin line) before vanishing again at T_x (■).

terisk) is a concurrent vanishing of $B^{(2)}$ (thick line). A more detailed analysis shows that this does not result from edge inductance, but reflects an increased surface barriers in the vortex solid due to enhanced c-axis correlations [28], which enhances the current flow symmetry. To break this enhanced symmetry below T_m and probe the edge inductance we add a small dc current bias. In its presence a finite second harmonic signal (Fig. 4(c), thin line) subsists below melting before vanishing at T_x (square). The detection of T_x below melting allows to extract the edge resistance within the solid phase (Fig. 4(b), squares), which fits perfectly and extrapolates the transport resistance. Consequently, we find that the edge resistance measured either in transport or by the edge inductance at T_x shows no pronounced feature at melting once the c-axis contribution is removed by current contact irradiation. This suggests that in highly anisotropic materials, such as BSCCO, the reported resistive melting step originates mostly from the loss of c-axis correlations through a simultaneous sublimation into a pancake gas [20, 40, 41]. In contrast, the loss of inter-vortex correlations within the a-b planes at melting has no significant mark in the vortex flow rate through the edges.

Finally, our complete set of data is given by dotted lines in Fig. 2 that represent contours of equal edge resistance (*i.e.* measured at the same frequency) spanning three and a half orders of magnitude in the $H-T$ phase diagram. It is evident that the exponential temperature dependence of the edge resistance becomes steeper on approaching the melting as the contour lines bunch together. This is attributed to the enhanced stiffness of the pancake vortex stacks. Nevertheless, we do not find a singular behavior at melting which would have manifested itself in overlapping contour lines. On the contrary, once the c-axis contribution is eliminated the edge resistance in solid joins smoothly that of the liquid.

In summary, the spatial distribution of transport current and its frequency dependence show that the T_x line, tentatively ascribed to a phase transition of vortex matter in BSCCO, is rather an electrodynamic transition. Consequently, in the wide field and temperature range that lies below the T_x line the inductance of the sample edges, usually dismissed in transport experiments, dominates the current flow and causes ac displacement of vortices across the bulk without crossing the sample edges. At T_x, the inductive part of the edge impedance equals the resistive part, which allows measurement of resistance down to two orders of magnitude below the transport noise. In the vicinity of the melting transition, we find that once the c-axis contribution is eliminated via ion irradiation of the current contacts, the edge resistance shows no sharp features at melting.

We thank H. Shtrikman for GaAs heterostructures and M. Konczykowski for ion irradiation. This work was supported by the German-Israeli Foundation (GIF). HB acknowledges the support of the Adams Fellowship Program of the Israel Academy of Sciences and Humanities and EZ the US-Israel Binational Science Foundation (BSF).

* Electronic address: haim.beidenkopf@weizmann.ac.il

[1] G. Blatter *et al.*, *Rev. Mod. Phys.* **66**, 1125 (1994).
[2] G. P. Mikitik and E. H. Brandt, *Phys. Rev. B* **68**, 054509 (2003).
[3] E. Zeldov *et al.*, *Nature* **375**, 373 (1995).
[4] A. Schilling *et al.*, *Phys. Rev. Lett.* **78**, 4833 (1997).
[5] H. Safar *et al.*, *Phys. Rev. Lett.* **68**, 2672 (1992).
[6] C. J. van der Beek *et al.*, *Physica C* **195**, 307 (1992).
[7] H. Beidenkopf *et al.*, *Phys. Rev. Lett.* **95**, 257004 (2005).
[8] H. Beidenkopf *et al.*, *Phys. Rev. Lett.* **98**, 167004 (2007).
[9] D. T. Fuchs *et al.*, *Phys. Rev. Lett.* **80**, 4971 (1998).
[10] E. Forgan, *Czech. J. Phys* **46**, 1571 (1996).
[11] T. Shibauchi *et al.*, *Phys. Rev. Lett.* **83**, 1010 (1999).
[12] Y. Ando and K. Nakamura, *Phys. Rev. B* **59**, R11661 (1999).
[13] K. Kimura *et al.*, *Physica B* **284**, 717 (2000).

[14] Y. Eltsev *et al.*, *Physica C* **341**, 1107 (2000).
[15] R. Sugano *et al.*, *Physica B* **284**, 803 (2000).
[16] Y. Nonomura and X. Hu, *Phys. Rev. Lett.* **86**, 5140 (2001).
[17] D. Li, P. Lin and B. Rosenstein, *Physica C* **468**, 1245 (2008).
[18] J. Dietel and H. Kleinert, *Phys. Rev. B* **79**, 014512 (2009).
[19] A. V. Samoilov *et al.*, *Phys. Rev. Lett.* **76**, 2798 (1996).
[20] L. I. Glazman and A. E. Koshelev, *Phys. Rev. B* **43**, 2835 (1991).
[21] B. Horovitz and T. R. Goldin, *Phys. Rev. Lett.* **80**, 1734 (1998).
[22] H. M. Carruzzo and C. C. Yu, *Philos. Mag. B* **77**, 1001 (1998).
[23] E. Frey, D. R. Nelson and D. S. Fisher, *Phys. Rev. B* **49**, 9723 (1994).
[24] M. Feigel'man, V. Geshkenbein and A. Larkin, *Physica C* **167**, 177 (1990).
[25] C. P. Bean and J. D. Livingston, *Phys. Rev. Lett.* **12**, 14 (1964).
[26] E. Zeldov *et al.*, *Phys. Rev. Lett.* **73**, 1428 (1994).
[27] D. T. Fuchs *et al.*, *Nature* **391**, 373 (1998).
[28] L. Burlachkov, A. E. Koshelev and V. M. Vinokur, *Phys. Rev. B* **54**, 6750 (1996).
[29] E. H. Brandt, G. P. Mikitik and E. Zeldov, *Phys. Rev. B* **74**, 094506 (2006).
[30] C. J. van der Beek and P. H. Kes, *Phys. Rev. B* **43**, 13032 (1991).
[31] D. G. Steel and J. M. Graybeal, *Phys. Rev. B* **45**, 12643 (1992).
[32] R. Busch *et al.*, *Phys. Rev. Lett.* **69**, 522 (1992).
[33] B. Khaykovich *et al.*, *Phys. Rev. B* **61**, R9261 (2000).
[34] D. R. Nelson and V. M. Vinokur, *Phys. Rev. Lett.* **68**, 2398 (1992).
[35] M. Konczykowski *et al.*, *Phys. Rev. B* **51**, 3957 (1995).
[36] T. Tamegai *et al.*, *J. Low Temp. Phys.* **117**, 1363 (1999).
[37] R. A. Doyle *et al.*, *Phys. Rev. Lett.* **77**, 1155 (1996).
[38] W. S. Seow *et al.*, *Phys. Rev. B* **53**, 14611 (1996).
[39] D. T. Fuchs *et al.*, *Phys. Rev. B* **54**, R796 (1996).
[40] D. T. Fuchs *et al.*, *Phys. Rev. B* **55**, R6156 (1997).
[41] S. Colson *et al.*, *Phys. Rev. Lett.* **90**, 137002 (2003).

3.4 Bulk Vortex Resistance at the Glass Transition

H. Beidenkopf, Y. Myasoedov, E. Zeldov, E.H. Brandt, G.P. Mikitik, T. Tamegai, T. Sasagawa and C. J. van der Beek. *Unpublished.*

Bulk vortex dynamics in $Bi_2Sr_2CaCu_2O_8$ crystals are studied in the vicinity of the thermodynamic second-order vortex glass transition. The resistance of the sample bulk, that in transport measurements is shunted by its edges, is extracted from the current distribution within the sample. The c-axis contribution to the resistance is eliminated utilizing ion-irradiated current contacts. We measure the bulk resistance in the vortex liquid phase, in the ordered solid phase, and across the melting transition. While both the liquid and ordered phases show critical behavior on approaching the glass transition, only the ordered phase shows a non-Ohmic resistance.

Much experimental effort has been invested in unveiling the thermodynamic vortex matter phase diagram and the dynamic behavior in the high-temperature superconductor $Bi_2Sr_2CaCu_2O_8$. One of the main challenges arises from the dominance of quenched disorder at low temperatures. The disorder impedes relaxation processes, resulting in a non-equilibrium hysteretic magnetization which obscures the thermodynamic ground state of the system. In addition, strong pinning results in a resistance that decreases exponentially with cooling, which conceals the low-temperature vortex dynamics. Vortex 'shaking' technique was recently shown to relax the vortex matter towards equilibrium [91, 92], revealing both an inverse melting extension of the first-order melting transition, T_m [21], and a second-order vortex glass transition, T_g, that bisects it [93, 94]. The resulting phase diagram consists of high-field vortex liquid and vortex glass phases. At low fields the glass transition separates the Bragg glass phase at low temperatures from a thermally depinned variant of it, possibly a vortex lattice, that calls for further elucidation. We characterize the bulk vortex dynamics within the liquid and lattice phases in general, and specifically close to the glass line.

The thermodynamic magnetization and dynamic resistive response of several $Bi_2Sr_2CaCu_2O_8$ single crystals of typical size $1000 \times 350 \times 20$ μm^3 were investigated. The local magnetization was measured with an array of 10×10 μm^2 Hall sensors fabricated in a two-dimensional electron gas trapped at the interface of GaAs/AlGaAs heterostructure. At low temperatures an in-plane shaking field of 350 Oe and 10 Hz was applied. Though the sample resistance was measured directly via ac transport, we find it inadequate for reasons detailed below. We, therefore, used the Hall sensor array to monitor simultaneously the current distribution within the sample, which we extract from the ac magnetic

field profile induced by the transport current according to the Biot-Savart law. A simple model for the sample electrodynamics [90] enables us to reproduce the bulk (and edge [95]) resistance from the sharp changes in the current distributions we detect.

The glass transition is manifested by a kink in the local magnetization, demonstrated in Fig. 3.2(a,b) at fields lying both above and below the melting line, respectively, from which a linear slope, α, was subtracted for clarity. It occurs reversibly on the cooling and heating branches, indicating that it is an equilibrium behavior, due to the application of a simultaneous in-plane ac field component. In the crossing-lattices state, the in-plane component of the response to an inclined field is in the form of a Josephson vortex lattice [13, 96, 97]. The Josephson vortices are formed between the CuO_2 planes. During the ac cycle of the in-plane field Josephson vortices intersect the pancake vortex stacks at random. The strong short-range attraction between pancake and Josephson vortices [13, 70] agitates pancake vortices, allowing them to assume their equilibrium configuration.

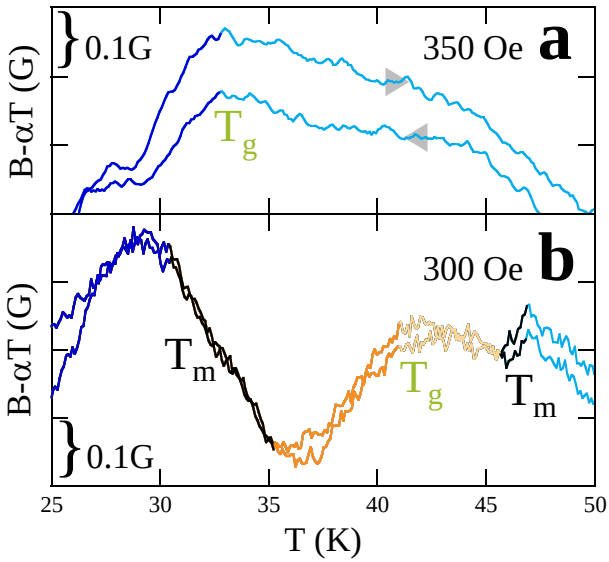

Fig. 3.2: *Reversible local magnetization measurements in the presence of an in-plane shaking field taken above (a) and below (b) the first-order melting line, T_m. Both show a signature of a second-order glass transition, T_g.*

At the high field of Fig. 3.2(a), the second-order transition at $T_g \approx 33$ K separates a vortex liquid phase above it from an amorphous vortex glass below. At the slightly lower field, presented in Fig. 3.2(b), the magnetic response of the sample is completely altered. Two first-order magnetization steps of opposite sign appear reversibly. They signal the high-temperature vortex solidification from a liquid phase to an ordered one [39], followed by inverse melting back to an amorphous phase [21]. A kink in the local reversible magnetization is detected at $T_g \approx 41$ K, manifesting a glass transition within the ordered region of the thermodynamic phase diagram, shown in Fig. 3.3.

Interestingly, in this particular sample the high and low field parts of the glass transition line terminate at two well-separated tricritical points on the melting line. In all previously measured $Bi_2Sr_2CaCu_2O_8$ samples this separation was below our experimental resolution [94]. As the phases involved are different above and below melting, there is no

reason for the critical points to be identical. The distinct behavior may be related to the slight oxygen under-doping of this sample, as opposed to optimally- and over-doped samples that we measured previously. This means, however, that between these two tricritical points the low-temperature Bragg glass phase melts directly to liquid.

Next, we discuss the vortex dynamics as the glass transition is approached from within the liquid and lattice phases. Theoretically, the glass transition, being of second-order, should give rise to a critical resistivity in its vicinity [98, 61]. Above T_g at current densities lower than the critical one, $j \sim T|T - T_g|^{\nu(d-1)}/\Phi_\circ$, the resistivity should be Ohmic and vanish as $\rho \sim |T - T_g|^{\nu(z+2-d)}$, with ν and z being characteristic critical exponents, and d the dimensionality of the system. At higher current densities it crosses to the generally non-Ohmic $\rho \sim j^{(z-d+2)/(d-1)}$. Further above from T_g, the resistance of the liquid phase should be Ohmic $\rho \sim e^{-U/T}$, while still reflecting vortex thermal activation over bulk energy barriers, U [59]. Within the Bragg glass phase, on the other hand, these bulk barriers are predicted to diverge with vanishing current, $U(j) = U_\circ j^{-\mu}$, with a critical exponent $\mu = 0.5$ [17, 99]. A thermally depinned lattice phase should thus have some intermediate or even Ohmic behavior [77].

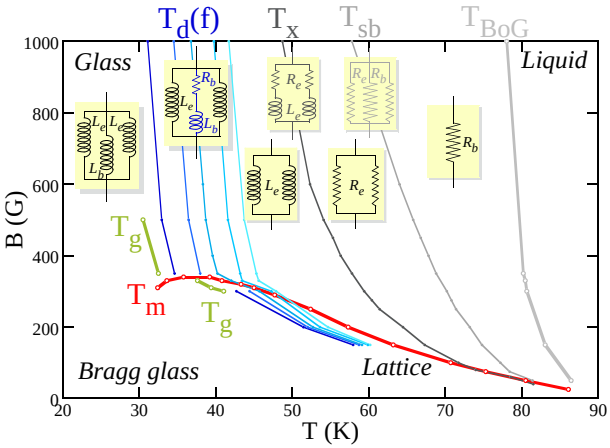

Fig. 3.3: *The thermodynamic vortex matter phase diagram in $Bi_2Sr_2CaCu_2O_8$ consists of a first-order melting T_m, and second-order glass transition T_g lines in pristine samples. The sample dynamics are dominated by bulk resistance at high temperatures, edge resistance below T_{sb}, edge inductance below T_x and bulk inductance below the frequency-dependent depinning line $T_d(f)$. Ion irradiation of the contact regions gives rise to the Bose glass transition T_{BoG}.*

Naively, this information can be directly inferred from transport measurements [100, 48]. However, the edge barriers [65, 66] that dominate the flow below the T_{sb} line (Fig. 3.3) [101, 67], the extreme material anisotropy due to its layered structure [63], and insufficient sensitivity render global transport measurements inadequate for this task. Alternatively, some information about the typical energy barriers involved in the vortex flow can be gained from studying the relaxation processes of the hysteretic magnetization [102], and the magnetic susceptibility [37, 45, 103]. However, these measurements are commonly taken with global probes, which again cannot distinguish between edge and bulk behavior.

Therefore, we devised a local method to extract the resistance of the sample from

changes in the current distribution inside it. The spatial resolution allows us to distinguish between bulk and edge contributions. This method was used previously to map the depinning transition, T_d, and the T_x line (Fig. 3.3). More recently, we used it to identify the role of the edge inductance in driving the T_x transition, which enabled us to quantitatively extract the resistance of the sample edges [95]. Here, we apply it to the sample bulk.

In addition, we eliminate the non-linear contribution of the c-axis resistance [63], and resolve the ambiguity in the actual depth through which current flows [62] by irradiating the volumes beneath the current contacts (colored in green in the schematic drawing of the sample in Fig. 3.4) while masking the central part of the sample which, thus, remains pristine. Samples were irradiated with a high dose of 1 GeV Pb ions in GANIL (Caen, France). Below the Bose glass transition, T_{BoG} (marked in Fig. 3.3), vortices pin to the columnar defects, induced along the ion tracks [32, 52]. This reduces the sample anisotropy in the irradiated regions [31], allowing current to penetrate throughout the sample thickness before it flows in the pristine central region. This irradiation scheme was indeed shown to result in a full current penetration and an Ohmic transport resistance below T_{BoG} [95].

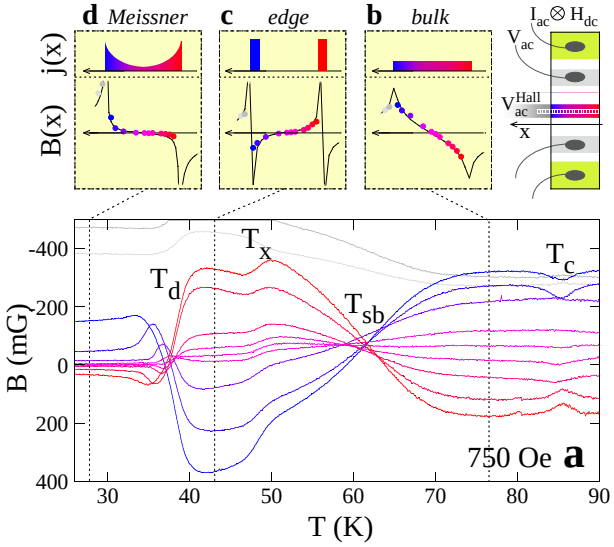

Fig. 3.4: *(a) The magnetic induction profile induced by the ac current flowing in the sample (setup shown schematically, green contacts were ion iraddiated). The uniform bulk flow at high temperatures (b) turns to edge flow below T_{sb} (c) and assumes a Meissner-like distribution that induces zero magnetic induction inside the sample below T_d (d).*

Figure 3.4(a) shows the dramatic changes in the measured ac magnetic profile across the sample, $B(x)$, induced by the flow patterns of the injected ac current, $j(x)$ [47]. While at high temperatures Biot-Savart relates the magnetic profile with a uniform current distribution (Fig. 3.4(b)), below T_{sb} the magnetic profile is inverted, indicating predominant edge flow (Fig. 3.4(c)). This is due to fast-increasing energetic edge barriers, which define an effective edge resistance, R_e. Below T_{sb} it becomes smaller than the bulk resistance, R_b. Below T_x it becomes even smaller than the inductance of the edges, L_e, which dominate the sample impedance [95]. Consequently, the pancake vortices hardly cross the edges, but merely redistribute within the sample to comply with the oscillating $B(x)$ profile.

The magnetic profile becomes antisymmetric, signifying an equal amount of current that flows on the opposite edges.

At yet lower temperatures current suddenly returns to the bulk while the magnetic signal vanishes, marking the depinning transition, T_d [47]. This happens because current flows in a Meissner-like distribution that induces zero ac magnetic field inside the sample (Fig. 3.4(d)). Accordingly, it was suggested that T_d is a phase transition, signifying the onset of bulk pinning which enhances the critical current and prevents flux redistribution inside the sample. In contrast, we claim that the depinning transition is rather an electrodynamic crossover, at which the bulk resistance equals the bulk inductance, $R_b(T_d) = 2\pi f L_b$. Consequently, below T_d the skin penetration depth becomes shorter than the sample width, which is why pancake vortices no longer manage to redistribute across the sample bulk.

This further suggests that the T_d transition has a frequency dependence from which the bulk resistance may be reproduced by substituting the effective bulk inductance, employed before in a similar manner with global ac susceptibility measurements [45, 103]. Taking into account both the self inductance of the bulk and its mutual inductance with the edges [90] yields $L_b = l\mu_\circ/4\pi = 80$ pH, where $l = 800$ μm is the separation between voltage contacts (for later comparison with transport results).

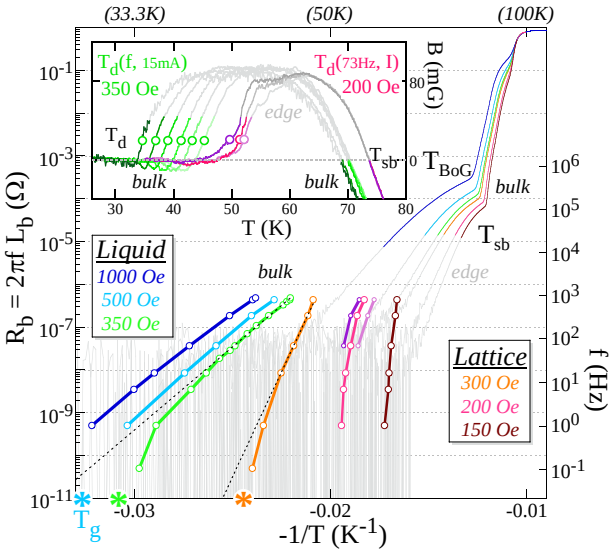

Fig. 3.5: *The bulk resistance extracted from $T_d(f)$ (thick lines) shows Arrhenius temperature dependence (dotted lines) before approaching the glass transition (∗). The edge resistance measured in transport below T_{sb} (grey thin lines) shunts the bulk one. Inset: Frequency dependence of T_d (1, 7, 37, 141, 371, 871 Hz at 15 mA) in the liquid phase (green), and current-amplitude dependence of T_d (10, 15, 20 mA at 73 Hz) in the lattice phase (orange).*

Indeed, the inset of Fig. 3.5 shows (green lines) that the vanishing of the induced magnetic signal, that marks T_d, occurs at increasingly higher temperatures with increasing the measurement frequency from 1 Hz to 1 kHz. In the main panel of the figure $T_d(f)$ is translated to the temperature dependence of the bulk resistance $2\pi f L_b$ at various applied dc fields (thick lines). Also shown in the figure are the transport resistances measured simultaneously at the respective fields (thin lines). The temperatures at which they turn grey

mark the T_{sb} transition, below which most of the current is carried by the sample edges. Therefore, the transport resistances reflect the edge resistances at these low temperatures, which indeed lie several orders of magnitude below the bulk ones. Furthermore, the resistances reproduced from the $T_d(f)$ lie 3.5 orders of magnitude below transport measurement noise floor (typically 10^{-7} Ω).

A straight line in Fig. 3.5 corresponds to an Arrhenius behavior, $R_b \sim e^{-U/T}$, with the line slope being the energy barrier, U. At the higher resistive levels we find good agreement with such an Arrhenius temperature dependence both at fields that lie above melting within the liquid phase (green), as well as below it within the lattice phase (orange), demonstrated by the dotted lines. However, at the lowest resistances measured, that correspond to a measurement frequency of 0.1 Hz, the resistance clearly deviates from the straight line. Moreover, this drop in resistance occurs once approaching the glass transition temperature (asterisks), extracted independently from dc magnetization in the presence of shaking. This sharp resistive drop with cooling may indeed signify a crossover from thermally activated to critical bulk resistance, $R_b \sim (T - T_g)^{\nu(z+2-d)}$. A much finer low frequency (temperature) mapping is required in order to extract the critical exponents.

Finally, we examine the $I-V$ characteristics in the liquid and lattice phases by reproducing their bulk resistances with different current amplitudes $R_b(T, I)$ through $T_d(f, I)$. At high fields, within the vortex liquid phase we find no dependence on the current amplitude which signifies Ohmic behavior. In contrast, at fields below the melting transition a clear current-amplitude dependence of T_d is observed, as demonstrated by violet lines in the inset of Fig. 3.5. The main panel further shows the temperature dependence of the resistance at these three current amplitudes (thick violet lines). This allows to extract the current dependence of the resistance at a given temperature which all three lines cross (about 54 K for the limited data set presented). Unfortunately, more data points from additional current amplitudes are required in order to reliably determine the functional dependence of the bulk resistance on current amplitude. Still, the data we have resembles more a linear current dependence of the bulk resistance rather than stretched exponential. If this indeed validates, it would give a strong indication that the phase above the glass transition and below melting is not Bragg glass.

In summary, we succeeded in measuring the bulk resistance from the current redistribution induced by the bulk skin effect. At low temperatures it is indeed orders of magnitude higher than the shunting edge resistance measured in transport. The bulk resistance drops on entering the critical region of the glass transition, deviating from the thermally-activated behavior seen at high temperatures. While we find Ohmic bulk resis-

tance within the liquid phase, it becomes non-Ohmic below melting. However, the current dependence there does not seem to correspond to the glassy one predicted for the Bragg glass phase.

4. Discussion

A novel phase transition was detected in the phase diagram of vortex matter in the high transition temperature superconductor $Bi_2Sr_2CaCu_2O_8$ [93]. It manifests itself by a reversible cusp in the local magnetization in the presence of vortex shaking, indicating its second-order nature. While the detection of the phase transition at high vortex densities seems to resolve the long lasting uncertainty regarding the thermodynamic origin of the amorphous glassy phase [19, 60], its occurrence below melting within the Bragg glass region of the phase diagram was not anticipated. Prior to its detection under equilibrium conditions the Bragg glass phase was widely considered to be stable under thermal fluctuation so long as topological excitations, which lead to vortex melting, are excluded [16, 17].

Studying the oxygen doping dependence of the phase diagram [94], we found that the glass transition line follows unexpectedly the anisotropy scaling transformation of the thermally induced part of the melting line [6, 82, 84, 85]. This naive scaling law does not take into consideration the effects of disorder, and indeed breaks at lower temperatures once disorder becomes relevant for vortex melting. Nevertheless, it does hold for the glass transition, which we believe to be intimately related with the defect contents in the sample. We addressed this issue by initiating a study of the direct effect of the disorder strength on the glass line by increasing it gradually through proton irradiation. However, this study is still in a preliminary stage in which we have demonstrated that proton irradiation greatly enhances the role of disorder in driving the melting transition, but did not get to investigate systematically its effect on the glass transition.

We then studied the vortex dynamics in the vicinity of the glass transition and above it. A novel indirect technique was implemented for measuring the sample edge and bulk resistances independently. We thus identified the edge inductance as driving the T_x transition, which is accordingly electrodynamic [95]. The bulk inductance was later used as a sensitive probe for measuring the bulk resistance through its skin effect. The bulk resistance showed a critical behavior in the vicinity of the thermodynamic glass transition, which strongly supports its second-order nature. While verifying the Ohmic $I - V$ char-

acteristics of the vortex liquid phase, this method showed non-Ohmic behavior for the presumably lattice phase below melting and above the glass transition. However, preliminary results suggest that this non-linearity is not of a glassy type, and in particular does not match the predictions made for the vortex flow within the Bragg glass phase [99]. One other project that did not get to completion involved samples with Corbino-disk contact geometry [72, 73] whose current contacts were ion irradiated [31, 53] as to eliminate both the effects due to sample-edges and nonuniform current penetration along the c-axis.

On a broader perspective, our measurements have shown that a critical behavior, apparently a glass transition of second-order, occurs across the phase diagram. It follows a basic scaling with anisotropy, shared also by the melting line. The vortex dynamics is also in support of a critical region in its vicinity, and the $I - V$ characteristics above it are Ohmic for the liquid phase and non-Ohmic but non-glassy below melting and above the glass transition, suggestive of thermal depinning. Yet, additional aspects should be investigated, such as direct determination of the spatial correlations either via diffraction or with a scanning probe technique, heat capacity measurements for validating the thermodynamic nature of the transition, dependence on defect contents, etc., parallel to theoretical effort, in order to thoroughly identify the exact nature of the novel glass transition.

References

[1] Bardeen, J., Cooper, L. N., and Schrieffer, J. R. *Phys. Rev.* **108**, 1175 (1957).

[2] Tinkham, M. *Introduction to Superconductivity.* McGraw-Hill, (1975).

[3] Timusk, T. and Statt, B. *Rep. Prog. Phys.* **62**, 61 (1999).

[4] Gomes, K. K., Pasupathy, A. N., Pushp, A., Ono, S., Ando, Y., and Yazdani, A. *Nature* **447**, 569 (2007).

[5] Kohsaka, Y., Taylor, C., Wahl, P., Schmidt, A., Lee, J., Fujita, K., Alldredge, J. W., McElroy, K., Lee, J., Eisaki, H., Uchida, S., Lee, D., and Davis, J. C. *Nature* **454**, 1072 (2008).

[6] Khaykovich, B., Zeldov, E., Majer, D., Li, T. W., Kes, P. H., and Konczykowski, M. *Phys. Rev. Lett.* **76**, 2555 (1996).

[7] Meissner, W. and Ochsenfeld, R. *Naturwissenschaften* **21**, 787 (1933).

[8] Clem, J. R. *Phys. Rev. B* **43**, 7837 (1991).

[9] Bulaevskii, L. N. *Sov. Phys. JETP* **37**, 1133 (1973).

[10] Clem, J. R. and Coffey, M. W. *Phys. Rev. B* **42**, 6209 (1990).

[11] Blatter, G., Feiglman, M. V., Geshkenbein, V. B., Larkin, A. I., and Vinokur, V. M. *Rev. Mod. Phys.* **66**, 1125 (1994).

[12] Bulaevskii, L. N., Ledvij, M., and Kogan, V. G. *Phys. Rev. B* **46**, 366 (1992).

[13] Koshelev, A. E. *Phys. Rev. Lett.* **83**, 187 (1999).

[14] Abrikosov, A. A. *JETP* **5**, 1174 (1957).

[15] Larkin, A. I. and Ovchinnikov, Y. N. *Journal of Low Temperature Physics* **34**, 409 (1978).

[16] Giamarchi, T. and Doussal, P. L. *Phys. Rev. Lett.* **72**, 1530 (1994).

[17] Nattermann, T. *Phys. Rev. Lett.* **64**, 2454 (1990).

[18] Chikumoto, N., Konczykowski, M., Motohira, N., and Malozemoff, A. P. *Phys. Rev. Lett.* **69**, 1260 (1992).

[19] Cubitt, R., Forgan, E. M., Yang, G., Lee, S. L., Paul, D. M., Mook, H. A., Yethiraj, M., Kes, P. H., Li, T. W., Menovsky, A. A., Tarnawski, Z., and Mortensen, K. *Nature* **365**, 407 (1993).

[20] Khaykovich, B., Konczykowski, M., Zeldov, E., Doyle, R. A., Majer, D., Kes, P. H., and Li, T. W. *Phys. Rev. B* **56**, R517 (1997).

[21] Avraham, N., Khaykovich, B., Myasoedov, Y., Rappaport, M., Shtrikman, H., Feldman, D. E., Tamegai, T., Kes, P. H., Li, M., Konczykowski, M., van der Beek, K., and Zeldov, E. *Nature* **411**, 451 (2001).

[22] Ertas, D. and Nelson, D. R. *Physica C* **272**, 79 (1996).

[23] Koshelev, A. E. and Vinokur, V. M. *Phys. Rev. B* **57**, 8026 (1998).

[24] Geshkenbein, V. B., Ioffe, L. B., and Larkin, A. I. *Phys. Rev. B* **48**, 9917 (1993).

[25] Bean, C. P. *Rev. Mod. Phys.* **36**, 31 (1964).

[26] Paltiel, Y., Zeldov, E., Myasoedov, Y., Rappaport, M. L., Jung, G., Bhattacharya, S., Higgins, M. J., Xiao, Z. L., Andrei, E. Y., Gammel, P. L., and Bishop, D. J. *Phys. Rev. Lett.* **85**, 3712 (2000).

[27] Chikumoto, N., Konczykowski, M., Motohira, N., Kishio, K., and Kitazawa, K. *Physica C* **185**, 2201 (1991).

[28] López, D., Krusin-Elbaum, L., Safar, H., Righi, E., de la Cruz, F., Grigera, S., Feild, C., Kwok, W. K., Paulius, L., and Crabtree, G. W. *Phys. Rev. Lett.* **80**, 1070 (1998).

[29] Lombardo, L. W., Mitzi, D. B., Kapitulnik, A., and Leone, A. *Phys. Rev. B* **46**, 5615 (1989).

[30] Konczykowski, M., Rullier-Albenque, F., Yacoby, E. R., Shaulov, A., Yeshurun, Y., and Lejay, P. *Phys. Rev. B* **44**, 7167 (1991).

[31] Doyle, R. A., Seow, W. S., Yan, Y., Campbell, A. M., Mochiku, T., Kadowaki, K., and Wirth, G. *Phys. Rev. Lett.* **77**, 1155 (1996).

[32] Nelson, D. R. and Vinokur, V. M. *Phys. Rev. Lett.* **68**, 2398 (1992).

[33] Bednorz, J. G. and Müller, K. A. *Z. Phys. B* **64**, 189 (1986).

[34] Kierfeld, J. and Vinokur, V. *Phys. Rev. B* **69**, 24501 (2004).

[35] Li, D. and Rosenstein, B. *Phys. Rev. Lett.* **90**, 167004 (2003).

[36] Mikitik, G. P. and Brandt, E. H. *Phys. Rev. B* **68**, 054509 (2003).

[37] Gammel, P. L., Schneemeyer, L. F., and Bishop, D. J. *Phys. Rev. Lett.* **66**, 953 (1991).

[38] Safar, H., Gammel, P. L., Huse, D. A., and Bishop, D. J. *Phys. Rev. Lett.* **69**, 824 (1992).

[39] Zeldov, E., Majer, D., Konczykowski, M., Geshkenbein, V. B., Vinokur, V. M., and Shtrikman, H. *Nature* **375**, 373 (1995).

[40] Brandt, E. H. *Phys. Rev. Lett.* **63**, 1106 (1989).

[41] Colson, S., Konczykowski, M., Gaifullin, M. B., Matsuda, Y., Gierłowski, P., Li, M., Kes, P. H., and van der Beek, C. J. *Phys. Rev. Lett.* **90**, 137002 (2003).

[42] Lee, S. L., Zimmermann, P., Keller, H., Warden, M., Savić, I. M., Schauwecker, R., Zech, D., Cubitt, R., Forgan, E. M., Kes, P. H., Li, T. W., Menovsky, A. A., and Tarnawski, Z. *Phys. Rev. Lett.* **71**, 3862 (1993).

[43] Fuchs, D. T., Doyle, R. A., Zeldov, E., Majer, D., Seow, W. S., Drost, R. J., Tamegai, T., Ooi, S., Konczykowski, M., and Kes, P. H. *Phys. Rev. B* **55**, R6156 (1997).

[44] Daemen, L. L., Bulaevskii, L. N., Maley, M. P., and Coulter, J. Y. *Phys. Rev. Lett.* **70**, 1167 (1993).

[45] van der Beek, C. J., Indenbom, M. V., Berseth, V., Li, T. W., and Benoit, W. *J. Low Temp. Phys.* **105**, 1047 (1996).

[46] Dewhurst, C. D. and Doyle, R. A. *Phys. Rev. B* **56**, 10832 (1997).

[47] Fuchs, D. T., Zeldov, E., Tamegai, T., Ooi, S., Rappaport, M., and Shtrikman1, H. *Phys. Rev. Lett.* **80**, 4971 (1998).

[48] Koch, R. H., Foglietti, V., Gallagher, W. J., Koren, G., Gupta, A., and Fisher, M. P. A. *Phys. Rev. Lett.* **63**, 1511 (1989).

[49] Matsuda, Y., Gaifullin, M. B., Kumagai, K., Kosugi, M., and Hirata, K. *Phys. Rev. Lett.* **78**, 1972 (1997).

[50] Yamaguchi, Y., Rajaram, G., Shirakawa, N., Mumtaz, A., Obara, H., Nakagawa, T., and Bando, H. *Phys. Rev. B* **63**, 014504 (2000).

[51] Giamarchi, T. and Doussal, P. L. *Phys. Rev. B* **52**, 1242 (1995).

[52] Konczykowski, M., Chikumoto, N., Vinokur, V. M., and Feigelman, M. V. *Phys. Rev. B* **51**, 3957 (1995).

[53] Seow, W. S., Doyle, R. A., Campbell, A. M., Balakrishnan, G., Paul, D., Kadowaki, K., and Wirth, G. *Phys. Rev. B* **53**, 14611 (1996).

[54] Koshelev, A. E. and Vinokur, V. M. *Phys. Rev. Lett.* **73**, 3580 (1994).

[55] Balents, L., Marchetti, M. C., and Radzihovsky, L. *Phys. Rev. B* **57**, 7705 (1998).

[56] Ryu, S., Hellerqvist, M., Doniach, S., Kapitulnik, A., and Stroud, D. *Phys. Rev. Lett.* **77**(25), 5114 (1996).

[57] Olson, C. J., Reichhardt, C., and Nori, F. *Phys. Rev. Lett.* **81**(17), 3757 (1998).

[58] Le Doussal, P. and Giamarchi, T. *Phys. Rev. B* **57**, 11356–11403 (1998).

[59] Koshelev, A. E. *Phys. Rev. Lett.* **76**, 1340 (1996).

[60] Safar, H., Gammel, P., Bishop, D., Mitzi, D., and Kapitulnik, A. *Phys. Rev. Lett.* **68**, 2672 (1992).

[61] Nattermann, T. and Scheidl, S. *Advances in Physics* **49**, 607 (2000).

[62] Busch, R., Ries, G., Werthner, H., Kreiselmeyer, G., and Saemann-Ischenko, G. *Phys. Rev. Lett.* **69**, 522 (1992).

[63] Khaykovich, B., Fuchs, D. T., Teitelbaum, K., Myasoedov, Y., Zeldov, E., Tamegai, T., Ooi, S., Konczykowski, M., Doyle, R. A., and Rycroft, S. F. W. R. *Phys. Rev. B* **61**, R9261 (2000).

[64] Braude, V. and Stern, A. *Phys. Rev. B* **67**, 064501 (2003).

[65] Zeldov, E., Larkin, A. I., Geshkenbein, V. B., Konczykowski, M., Majer, D., Khaykovich, B., Vinokur, V. M., and Shtrikman, H. *Phys. Rev. Lett.* **73**, 1428 (1994).

[66] Bean, C. P. and Livingston, J. D. *Phys. Rev. Lett.* **12**, 14 (1964).

[67] Fuchs, D. T., Zeldov, E., Rappaport, M., Tamegai, T., Ooi, S., and Shtrikman, H. *Nature* **391**, 373 (1998).

[68] Willemin, M., Schilling, A., Keller, H., Rossel, C., Hofer, J., Welp, U., Kwok, W. K., Olsson, R. J., and Crabtree, G. B. *Phys. Rev. Lett.* **81**, 4236 (1998).

[69] Mikitik, G. P. and Brandt, E. H. *Phys. Rev. B* **69**, 134521 (2004).

[70] Perkins, G. K., Caplin, A. D., and Cohen, L. F. *Supercond. Sci. Technol.* **18**, 1290 (2005).

[71] Fuchs, D. T., Zeldov, E., Majer, D., Doyle, R. A., Tamegai, T., Ooi, S., and Konczykowski, M. *Phys. Rev. B* **54**, R796 (1996).

[72] Mazilu, A., Safar, H., López, D., Kwok, W. K., Crabtree, G. W., Guptasarma, P., and Hinks, D. G. *Phys. Rev. B* **58**, R8913 (1998).

[73] Rycroft, S. F. W. R., Doyle, R. A., Fuchs, D. T., Zeldov, E., Drost, R. J., Kes, P. H., Tamegai, T., Ooi, S., and Foord, D. T. *Phys. Rev. B* **60**, R757 (1999).

[74] Marchetti, M. C. and Nelson, D. R. *Phys. Rev. B* **59**, 13624 (1999).

[75] Banerjee, S. S., Goldberg, S., Soibel, A., Myasoedov, Y., Rappaport, M., Zeldov, E., de la Cruz, F., van der Beek, C. J., Konczykowski, M., Tamegai, T., and Vinokur, V. M. *Phys. Rev. Lett.* **93**, 97002 (2004).

[76] Abulafia, Y., McElfresh, M., Shaulov, A., Yeshurun, Y., Paltiel, Y., Majer, D., Shtrikman, H., and Zeldov, E. *App. Phys. Lett.* **72**, 2891 (1998).

[77] Luo, M.-B., Hu, X., and Vinokur, V. cond-mat 0902.0858v1.

[78] Li, D., Rosenstein, B., and Vinokur, V. *J. Supercond. Novel Mag.* **19**, 369 (2007).

[79] Dietel, J. and Kleinert, H. *Phys. Rev. B* **79**, 014512 (2009).

[80] Hanaguri, T., Tsuboi, T., Maeda, A., Nishizaki, T., Kobayashi, N., Kotaka, Y., Shimoyama, J., and Kishio, K. *Physica C* **256**, 111 (1996).

[81] Kes, P., Pastoriza, H., Li, T., Cubitt, R., Forgan, E., Lee, S., Konczykowski, M., Khaykovich, B., Majer, D., Fuchs, D., and Zeldov, E. *J. Phys. I* **6**, 2327 (1996).

[82] Ooi, S., Shibauchi, T., and Tamegai, T. *Physica C* **302**, 257 (1998).

[83] Li, T. W., Menovsky, A. A., Franse, J. J. M., and Kes, P. H. *Physica C* **257**, 179 (1996).

[84] Klemm, R. A. and Clem, J. R. *Phys. Rev. B* **21**, 1868 (1980).

[85] Blatter, G., Geshkenbein, V. B., and Larkin, A. I. *Phys. Rev. Lett.* **68**, 875 (1992).

[86] Civale, L., Marwick, A. D., McElfresh, M. W., Worthington, T. K., Malozemoff, A. P., Holtzberg, F. H., Thompson, J. R., and Kirk, M. A. *Phys. Rev. Lett.* **65**, 1164 (1990).

[87] Summers, G. P., Burke, E. A., and Chrisey, D. B. *App. Phys. Lett.* **55**, 1469 (1989).

[88] Morozov, N., Zeldov, E., Majer, D., and Konczykowski, M. *Phys. Rev. B* **54**, R3784 (1996).

[89] Kim, D. H., Leea, T. W., Leea, C. W., Ha, D. H., and Shim, S. Y. *Physica C* **383**, 23 (2002).

[90] Brandt, E. H., Mikitik, G. P., and Zeldov, E. *Phys. Rev. B* **74**, 094506 (2006).

[91] Willemin, M., C. Rossel, J. H., Keller, H., Erb, A., and Walker, E. *Phys. Rev. B* **58**, R5940 (1998).

[92] Brandt, E. H. and Mikitik, G. P. *Physica C* **408**, 514 (2004).

[93] Beidenkopf, H., Avraham, N., Myasoedov, Y., Shtrikman, H., Zeldov, E., Rosenstein, B., Brandt, E. H., and Tamegai, T. *Phys. Rev. Lett.* **95**, 257004 (2005).

[94] Beidenkopf, H., Verdene, T., Myasoedov, Y., Shtrikman, H., Zeldov, E., Rosenstein, B., Li, D., and Tamegai, T. *Phys. Rev. Lett.* **98**, 167004 (2007).

[95] Beidenkopf, H., Myasoedov, Y., Zeldov, E., Brandt, E., Mikitik, G., Tamegai, T., Sasagawa, T., and van der Beek, C. *Submitted to Phys. Rev. Lett.* .

[96] Bolle, C. A., Gammel, P. L., Grier, D. G., Murray, C. A., Bishop, D. J., Mitzi, D. B., and Kapitulnik, A. *Phys. Rev. Lett.* **66**, 112 (1991).

[97] Grigorenko, A., Bending, S., Tamegai, T., Ooi, S., and Henini, M. *Nature* **414**, 728 (2001).

[98] Fisher, M. P. A. *Phys. Rev. Lett.* **62**, 1415 (1989).

[99] Giamarchi, T. and Doussal, P. L. *Phys. Rev. B* **55**, 6577 (1997).

[100] Fuchs, D. T., Doyle, R. A., Zeldov, E., Rycroft, S. F. W. R., Tamegai, T., Ooi, S., Rappaport, M. L., and Myasoedov, Y. *Phys. Rev. Lett.* **81**, 3944 (1998).

[101] Burlachkov, L., Koshelev, A. E., and Vinokur, V. M. *Phys. Rev. B* **54**, 6750 (1996).

[102] van der Beek, C., Kes, P., Maley, M., Menken, M., and A.A.Menovsky. *Physica C* **195**, 307 (1992).

[103] Steel, D. G. and Graybeal, J. M. *Phys. Rev. B* **45**, 12643 (1992).

סיכום

החומר המערבולתי במוליך העל בעל טמפרטורת המעבר הגבוהה $Bi_2Sr_2CaCu_2O_8$ מציע מערכת בה אינטראקציות, תנודות תרמיות ואי-סדר מתחרים בצמידות, ומביאים למתווה פאזות מורכב. כבר בשלב מוקדם תפיסת שריג המערבולות בעל הסדר המושלם ננטשה לטובת פאזת זכוכית הבראג, המסודרת למחצה. תנודות תרמיות בטמפרטורות גבוהות וניעוץ אקראי בטמפרטורות נמוכות וצפיפות מערבולות גבוהה מוסיפות לערער גם את יציבותה של פאזת זכוכית הבראג, ומביאים לתצורת מערבולות חסרת סדר. אנו מצאנו עדות למעבר-פאזה זכוכיתי חדש מסדר שני בתגובה המגנטית המקומית, שנהייתה הפיכה על-ידי הפעלת ניעור מערבולתי. הוא מוסיף חלוקה למתווה הפאזות לסך של ארבע פאזות שונות: בצפיפות מערבולות גבוהה שוכנות פאזות המערבולות הנוזלית והזכוכיתית חסרות הסדר. בשדות נמוכים קו הזכוכיתיות מפריד זכוכית בראג מגרסא מחולצת תרמית שלה, ויתכן שאף מציג מחדש סדר מרחבי ארוך-טווח של פאזת שריג מערבולות.

קו הזכוכיתיות החדש, ובפרט הפאזה המסקרנת של זכוכית הבראג המחולצת תרמית, קראו להמשך איפיון. על-כן, למדנו את התפתחות קו הזכוכיתיות עם אילוח חמצן, אשר מגביר את הצימוד בין השכבות מוליכות-העל של $Bi_2Sr_2CaCu_2O_8$, ומוסיף מרכזי ניעוץ. במפתיע מצאנו, שקו הזכוכיתיות עוקב אחר תלות פשוטה באנאיזוטרופיה, החופשייה מאי סדר, ביחד עם חלקו המושרה תרמית של קו ההמסה. תובנה נוספת הגיעה ממודל תיאורטי, שנמצא מתאר היטב את מתווה הפאזות הניסיונאי. מצאנו, שהפחתת האנאיזוטרופיה עם אילוח מפחיתה את תפקידו של הניעוץ, אף על פי שצפיפותו גדלה. להשלים זאת, החלנו בלמידת תלות מתווה הפאזות בצפיפות הפגמים, אשר הושפע עד מאוד מהקרנת פרוטונים.

דינאמיקת המערבולות בפאזות המחולצות תרמית ובסמיכות לגבול הפאזות הזכוכיתיות נלמדה בהמשך. התרומה הלא-ליניארית, העולה מהתגובה הדינאמית לאורך ציר-c, הוסרה באמצעות סכמת הקרנת יונים חדשנית. היות ורגישות מדידת טרנספורט אינה מספקת ללמידת ההתנגדות הקטנה-מעריכית בטמפרטורות כה נמוכות, הגינו גישה עקיפה למדידת התנגדות גוף הדוגמה. במסגרתה אנו מנטרים את התפלגות הזרם בדוגמה, הנובעת מההתחרות בין ההתנגדויות המופעלות-תרמית וההשראויות הגיאומטריות של גוף הדוגמה וקצוותיה. בתחילה אבחנו את טבעו החשמלי של המעבר T_x, מתחתיו השראות הקצוות שולטת בעכבת הדוגמה. לאחר מכן, השתמשנו בקו-החילוץ, T_d, מתחתיו רק יחס השראויות גוף הדוגמה וקצוותיה קובע את תבנית הזרימה, למציאת התנגדות גוף הדוגמה. שלא כמו נוזל המערבולות, הפאזה השריגית מביאה להתנגדות לא-אוהמית. מכל מקום נראה, שהתוצאות הראשוניות אינן מובילות להתנגדות זכוכיתית, החזויה לזכוכית הבראג. בנוסף, תלות ההתנגדות בטמפרטורה מצביעה על סטייה מהתנהגות מופעלת תרמית בהתקרב קו הזכוכיתיות הן מתוך פאזת הנוזל והן מהגביש, ומאותתת על התנהגות קריטית.